Journal of Volcanology and Geothermal Research 454 (2024) 108147

Contents lists available at ScienceDirect

Journal of Volcanology and Geothermal Research

journal homepage: www.journals.elsevier.com/journal-of-volcanology-and-geothermal-research

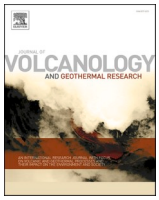

Co-eruptive, endogenous edifice growth, uplift during 4 years of eruption at Sangay Volcano, Ecuador

Pedro Alejandro Espín Bedón [a,*], Susanna K. Ebmeier [a], John R. Elliott [a], Tim J. Wright [a], Patricia Mothes [b], Valérie Cayol [c], Yasser Maghsoudi [a], Milan Lazecký [a], Daniel Andrade [b]

[a] COMET, School of Earth and Environment, University of Leeds, Leeds, UK
[b] Instituto Geofísico – Escuela Politécnica Nacional, Quito, Ecuador
[c] Université Clermont Auvergne, CNRS, IRD, OPGC, Laboratoire Magmas et Volcans, F-63000 Clermont-Ferrand, France

ARTICLE INFO

Keywords:
Sangay Volcano
Co-eruptive uplift
Endogenous growth

ABSTRACT

We report sustained uplift throughout Volcan Sangay's most recent period of eruption (2019–22), moderated only by transient excursions during some of its largest explosions. Volcan Sangay (Amazonia, Ecuador), has been erupting since 2019, impacting both local communities and distant cities with ash fall and lahars. We analyzed ascending and descending Sentinel-1 radar imagery, constructing a robust network of interferograms spanning this eruptive period to measure relative ground displacements across the volcano. Our time series reveals a consistent uplift pattern (~68 mm/yr) on the western and northern flanks of the volcano, which we attribute to volume increases in a body of magma located within the volcano's edifice beneath its western flank. This source appears to be vertically extensive, and is best fit by a quadrangular magma pathway, dipping towards the west and increasing in volume by 1.1×10^6 m^3 between 2019 and 2022. We additionally identify non-magmatic deformation, including subsidence of fresh deposits and downslope displacement (~50 mm/year) in the southeastern sector of the volcano. Co-eruptive uplift at Sangay is a rare observation of endogenous growth during an eruption and indicates that stratovolcano edifice stability is sensitive to both magma flux into the edifice and shallow controls on eruption rate.

1. Introduction

Measurements of deformation are a critical data set for monitoring volcanic eruptions (Dzurisin, 2007; Biggs et al., 2014; Spaans and Hooper, 2016; Biggs and Pritchard, 2017; Ebmeier et al., 2018; Pritchard et al., 2018), providing information about the timing, depth and potentially volume of subsurface magma movement. While satellite radar measurements now have the potential to provide near-global volcanic displacement data, measurements at some volcanoes are in practice limited by steep topography and rapid changes in the properties of surface scatterers associated with dense vegetation, frequent eruptions and gravity-driven flows (Pinel et al., 2011; Ebmeier et al., 2013a; Remy et al., 2015; Morales et al., 2017; Schaefer et al., 2019; Di Traglia et al., 2021). Here, we describe measurements of displacement made with Interferometric Synthetic Aperture Satellite Radar (InSAR) at Sangay volcano, Ecuador between 2015 and 2022. Sangay Volcano has been erupting semi-continuously since 1628 CE, has a very high relief (5.23 km) and is located on the edge of the Amazon rainforest, and therefore presents an exceptionally challenging case for InSAR measurements. However, InSAR measurements at Sangay Volcano are especially important given limitations in ground-based monitoring infrastructure and have the potential to provide critical information for understanding of the volcano's behavior, monitoring volcanic hazard and assessing associated risks to nearby communities. We test the impact of atmospheric corrections and network design for time series inversion with the aim of making robust displacement measurements that capture both long term trends and transient co-eruptive changes. We then use blind source separation methods to distinguish between magmatic and shallower-seated edifice displacements and explore the implications for magma supply during Sangay's current eruption. This allows us to locate the zone of magma storage within Sangay's edifice and quantify the volume changes during its current eruption an important parameter for monitoring and forecasting activity.

* Corresponding author.
E-mail address: eepabe@leeds.ac.uk (P.A. Espín Bedón).

https://doi.org/10.1016/j.jvolgeores.2024.108147
Received 26 April 2024; Received in revised form 24 July 2024; Accepted 27 July 2024
Available online 2 August 2024

1.1. Deformation during volcanic eruptions

The simplest conceptual model of how volcanoes deform during an eruption cycle comprises pre-eruptive uplift as magma accumulates in a shallow reservoir, followed by subsidence during an eruption as the reservoir empties (Sparks, 2003; Dzurisin, 2007; Wauthier et al., 2012; Chaussard et al., 2013; Biggs and Pritchard, 2017; Sparks and Cashman, 2017). When a reservoir empties gradually during a long-lived eruption (e.g., Hekla, Sigmundsson et al. (1992)), the elastic displacements may track the decrease in reservoir pressure. However, because the duration of co-eruptive subsidence is typically shorter than satellite radar repeat times (normally >6 days) co-eruptive subsidence typically appears instantaneous in InSAR time series (e.g. Euillades et al. (2017); Hamlyn et al. (2018); Himematsu et al. (2020)).

Sometimes pre-eruptive and co-eruptive displacements can cancel each other out (Fig. 1a), characterized by inflation followed by co-eruptive subsidence (e.g., Chaiten in Chile (Reath et al. 2019) or Galeras in Colombia (Parks et al. 2011)). Recharge of a reservoir and associated uplift (Fig. 1b) may begin immediately after an eruption (e.g. Cordón Caulle, Chile (Delgado et al., 2016; Euillades et al., 2017); Masaya in Guatemala (Stephens et al., 2017), Hekla in Iceland 2000 eruption (Ofeigsson et al., 2011), after an interval (e.g Láscar in Chile (Reath et al., 2019)), or not at all (e.g. Sinabung, Sumatra in 2010 eruption (Chaussard et al., 2013)). However, not all eruptions are preceded by measurable uplift, for example, when magma ascends rapidly from great depths (Ebmeier et al., 2013b), or when pre-eruptive pressurization occurs rapidly in a conduit (Salzer et al., 2014; Stephens et al., 2017) or reservoir (Cassidy et al., 2019; Morgado et al., 2019). The relationship between the volume of material erupted (V_E) and intruded volumes(V_I) estimated from inversion of geodetic data is also complex, especially where highly compressible bubble-rich magmas lead to under-estimation of V_I (Rivalta and Segall, 2008; Kilbride et al., 2016). However, accurately constraining the relative balance of these parameters is important for understanding the growth of volcanoes and interpreting their deformation.

If the long term intrusive flux into a sub-edifice reservoirs exceeds the time-averaged eruptive flux (Fig. 1c), the volcano will uplift, causing endogenous growth of the volcano's edifice. For example, at Mount Etna between 1975 and 1995, only 10% of the total magma erupted during the 1992 eruption (Allard, 1997). Co-eruptive intrusion into the neighbouring crust is a more typical feature of rift and/or hot spot volcanism (e.g. Pollard et al. (1983); Sigmundsson et al. (2010); Wright et al. (2012); Hamling et al. (2016); Dumont et al. (2018); Galetto (2023)). This phenomenon has also been well-documented in Hawai'i (Tilling and Dvorak, 1993; Garcia, 2015). For instance, during the period from 1976 to 1982, in Kilauea, the intruded volume accounted for 97% of the volume present at the eruption in 1983 (Cayol et al., 2000). Another example is Nyiragongo in 2002, where the erupted volume constituted between 6% to 16% of the intruded volume (Wauthier et al., 2012). Conversely, at some shields volcanoes like Piton de la Fournaise, the situation is reversed, with the volume of intruded magma comprising only 16% of the erupted magma volume (Dumont et al., 2024).

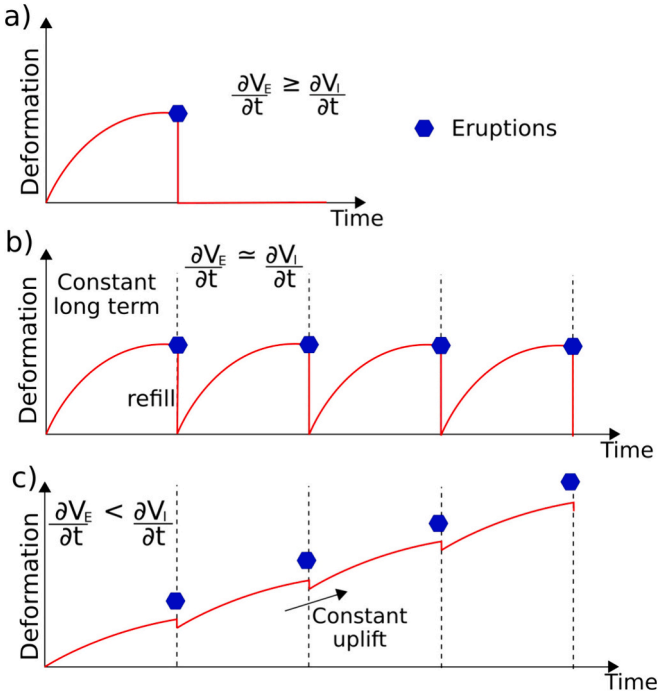

Fig. 1. Illustration of deformation cycles where eruption rate exceeds intrusion rate (a and b), and c) where long term intrusion rate exceeds eruption rate, adapted from (Biggs and Pritchard, 2017).

Observations of co-eruptive endogenous growth are rare at stratovolcanoes, perhaps because (1) there are still relatively few volcanoes where deformation has been measured over multiple cycles of eruption and (2) co-eruptive displacement measurements are particularly challenging at active stratovolcanoes. For example, Tungurahua volcano experienced both episodic (Biggs et al., 2010; Muller et al., 2018; Hickey et al., 2020) and long term uplift (Champenois et al., 2014; Morales et al., 2016) during its eruptive phase between 1999 and 2016 (Hidalgo et al., 2015; Mothes et al., 2015). At other volcanoes, persistent degassing or high thermal flux have been interpreted as evidence for endogenous growth (Francis et al., 1993), even in the absence of measurable accompanying displacement. In such cases, the depth at which degassed magma resides in the crust is unclear, and proposed alternatives include recycling in an active magma reservoir (Harris et al., 1999), the growth of deep cumulate complexes (Locke et al., 2003) or a shallow intrusion contributing to the growth of topography.

1.2. Measuring deformation at vegetated, active stratovolcanoes

Active stratovolcanoes present particular challenges for InSAR measurements (e.g. Westerhoff and Steyn-Ross (2020); Pinel et al. (2011); Ebmeier et al. (2013b); Remy et al. (2015); Morales et al., 2017. Steep topography results in phase decorrelation where differences in satellite position (perpendicular baseline) are large, as well as a loss of information due to the geometric distortions (foreshortening and layover) associated with side- looking radar geometry (Pinel et al., 2011, 2014). Frequent resurfacing during eruptions mean that the global Digital Elevation Models required to correct topographic phase contributions rarely capture current topography (e.g. Dualeh et al. (2021)), and also causes temporal decorrelation, limiting coherence and therefore measurements of displacement near the volcano's summit (Sandwell et al., 2007; Malinverni et al., 2014; Pinel et al., 2014; Jung et al., 2016; Biass et al., 2021). Seasonal snow cover and dense tropical vegetation also cause large variations in surface scattering properties and therefore limit satellite radar measurements (e.g. Amelung et al. (1999); Bathke et al. (2011); Arnold et al. (2018)).

Furthermore, tropospheric errors caused by variations in both hydrostatic pressure and the amount of water vapour are similar in magnitude, or even greater, than true deformation, especially at stratovolcanoes with high relief (Simons and Rosen, 2015). These are particularly problematic at stratovolcanoes due to (1) large variations in water vapour associated with high relief, (2) local turbulence and other orographic effects introduced by the volcano and therefore (3) major deviations between local atmospheric conditions and global weather models use to estimate and remove atmospheric phase contributions. The systematically poor coherence around a volcanic summit has an additional impact on the network design for time series inversion. Where longer timespan interferograms cannot be constructed, biases are introduced to time series built from shorter timespan interferograms in the form of a 'fading signal' (Ansari et al., 2020). The impact of this is

particularly severe over dense vegetation (Purcell et al., 2022).

1.3. Sangay volcano

Sangay volcano (5230 m) is the southernmost and most active of Ecuador's volcanoes (Monzier et al. 1999; Valverde et al., 2021; Vásconez et al., 2022), located in the Real Cordillera in Morona Santiago Province (2.002° latitude and 78.341° longitude, Fig. 2), 45 km southeast of Riobamba (population 264,000) and 40 km northwest of Macas city (population 25,414). It has an Amazonian climate, with lush vegetation on its lower flanks (Valverde, 2014) (Fig. 2c,d). Sangay is an andesitic volcano composed of three successive edifices (Fig. 2b), and the present cone ('Sangay III') started to form 14 ka. The earlier edifices ('Sangay I and II') were partially destroyed by huge landslides on their eastern flanks that caused large debris avalanches towards the Amazonian plains (Monzier et al. 1999; Hall et al., 2008; Valverde et al., 2021). The volcano lies in the Pastaza Depression, which is formed by reverse faults systems. The nearest faults, striking (N4°W ± 20°), and are located

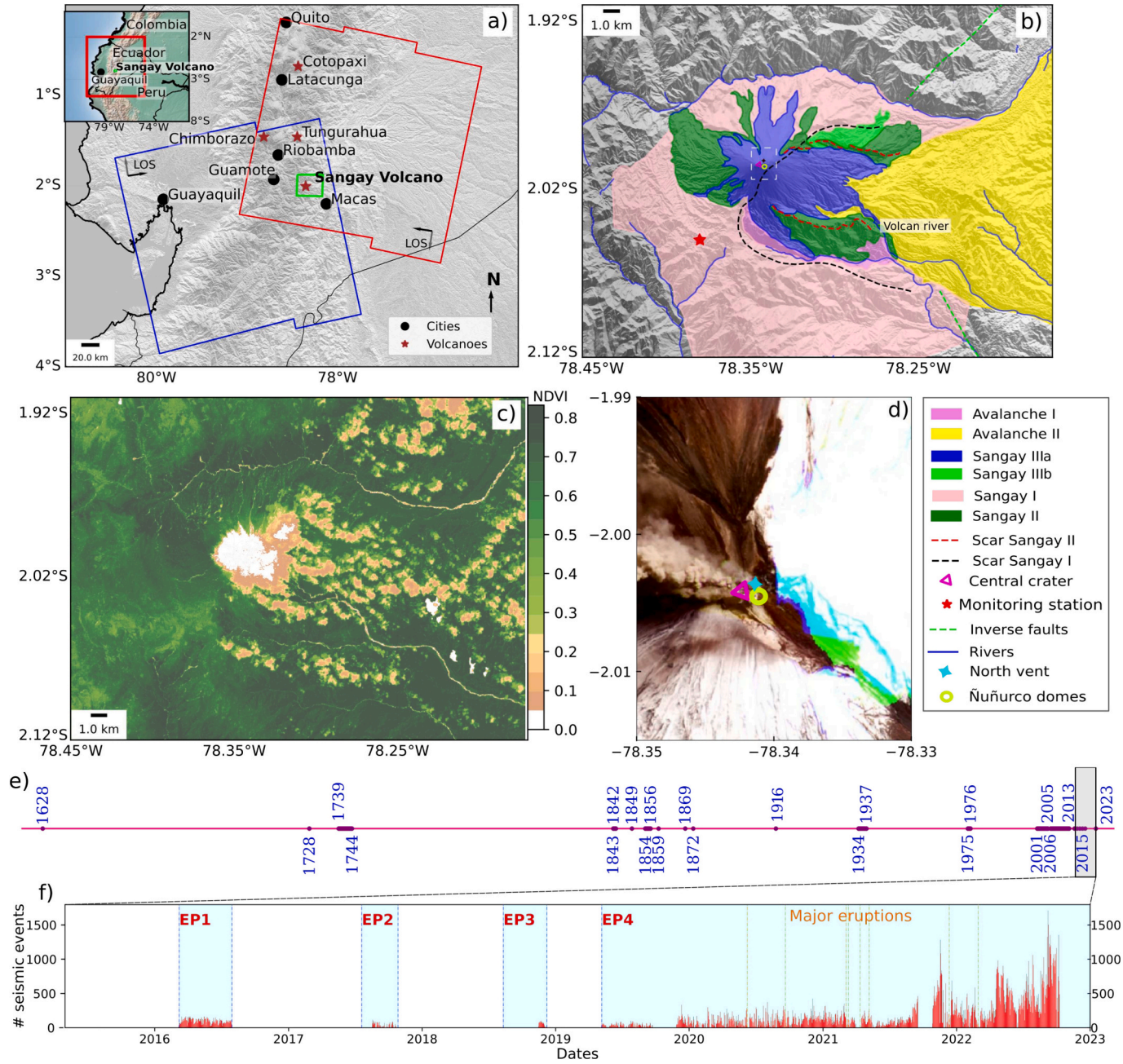

Fig. 2. a) Location of Sangay Volcano in Ecuador (green square), footprint of Sentinel-1 frames and look direction (blue ascending, red descending), b) Main geological settings and tectonic structure at Sangay (data from Valverde et al. (2021); Alvarado (2012), basemap: Copernicus Shade DEM. c) Normalised Difference Vegetation Index (NDVI) from Landsat. NDVI is generated by calculating the normalised difference between bands 8 and 4 of Lansat 10% cloudless composite, from 19 images between 2015-11-01 and 2022-07-31; d) Optical images from Planet Explorer, taken on August 25, 2020, depict the location of Ñuñurco dome, North vent and Central crater; e) Timeline from 1628 to 2023, depicting the historical eruptions recorded at the volcano, along with a zoomed-in view (f) of the period between 2016 and 2023. Red bars represent the seismic activity recorded by the monitoring station (IG-EPN), light blue background indicates eruptive periods (EP) defined by Vásconez et al., 2022, and dashed orange lines depict the most significant eruptions recorded within the study period of 2019 to 2023. These major eruptions are characterized by column heights exceeding 2 km, lava flows, and pyroclastic flows. (For interpretation of the references to colour in this figure legend, the reader is referred to the web version of this article.)

to the NE and SE approximately 8 km from the summit of the volcano (Eguez et al., 2003; Alvarado, 2012; Valverde et al., 2021).

Sangay has been erupting at least since the 17th century (Hall, 1977; Monzier et al. 1999; Hall et al., 2008; Valverde et al., 2021; Vásconez et al., 2022; Hidalgo et al., 2022). The active period since 1628 has been characterized by the formation of lava flows, with eruptive phases. Continuous eruptions with long pauses were reported from 1728 until 1916 and again from 1934 to the present (Fig. 2d). Eruptions from 2001 to 2020 have been divided into three eruptive periods (Vásconez et al., 2022) on the basis of the seismic catalog, thermal and ash emissions. The first period, from 2001 to 2013, consisted of low-explosivity activity. From 2015 to 2018, the behavior became "cyclical", characterized by phases of episodic eruptions (2 to 3 months) followed by periods of quiescence (9 to 13 months), characterized by low ash columns and Ñuñurco domes activity. The last eruptive period began on May 7, 2019, has been very intense in recent decades, and continues to the present date. This eruptive period has been characterized by discrete eruptive pulses that last a few days, followed by periods of lower level activity with similar duration. Seven episodes of increased activity (consisting of more explosive activity with lava flows and numerous lava front collapses) have been registered: June 8–9 and September 20, 2020, and on March 5–6, March 11, April 12, May 7, and December 12, 2021. Over the last two decades, Sangay's eruptions have originated primarily from Central Crater and the south-eastern domes (Ñuñurco domes), separated by 271 m distance (Fig. 2b). The activity from the Central Crater is explosive, characterized by the generation of eruptive plumes and ballistic blocks. The activity of the Ñuñurco domes has been effusive, with non-continuous emission of lava flows. In December 2021 a new vent appeared in the northern part of the volcano (Herrería, 2020; Hidalgo et al., 2022). Ash emissions, lahars from collapsing lava flows and pyroclastic density current (PDC) have had both direct and indirect impacts on surrounding populations (see Sangay volcano hazard map, Ordóñez et al. (2013)). Ash falls in 2020 affected both Guamote and even Guayaquil, located >100 km from the volcano. Lahars flowing to the south-east have impacted the main access roads to Macas city (Bernard et al., 2022) (see Fig. 2 to locate the towns).

The ground-based monitoring network at Sangay is limited by its remote location in the Ecuadorian Amazon and difficult access (Hidalgo et al., 2024). Understanding of recent activity is therefore dependent on optical and radar satellite imagery, thermal alerts and satellite derived sulphur dioxide measurements (e.g. Vásconez et al. (2022); Hidalgo et al. (2022)). However, our understanding of deformation at Sangay from InSAR is thus far incomplete, with many previous observations being inconclusive or ambiguous. For example, analysis of a single look direction (ascending ALOS imagery 2007–2011) is suggestive of downhill flank motion (Morales et al., 2017). Hidalgo et al. (2022) reported variable uplift between January and December 2021, with higher rates November–December 2021 and variations that seem to be associated with larger eruptions in December 2021.

In this work we make a systematic analysis of InSAR measurements at Sangay, focusing on displacements during the most recent eruptive period between 2019 and 2022 characterized by frequent explosions, ash and gas emissions, lava fountaining, lava flows and associated pyroclastic currents and secondary lahars (Vásconez et al., 2022; Hidalgo et al., 2022). We analyse both ascending and descending Sentinel-1 imagery, with the aims of (1) establishing the rate and potential source of apparent long-term uplift between 2015 and 2022, (2) determining the extent and properties of any down-slope motions on the edifice (3) testing whether major explosions in 2019–22 were accompanied by deformation.

2. Data and methods

2.1. Data

We analyse over 6 years of displacements at Sangay using InSAR time series from European Space Agency's Sentinel-1 SAR mission. The Sentinel-1 mission comprises a single polar-orbiting satellite (or constellation of two 2016–2022), operating at C-band (5.6 cm) wavelength, with a 5 × 20 m resolution in interferometric wide-swath (IW) mode.

We used the automatic interferometric processing of Sentinel-1 data (unwrapped and geocoded interferograms and coherence data in 56 m resolution) by the LiCSAR (Looking Into Continents from Space with Synthetic Aperture Radar) processor (Lazecky et al., 2020). LiCSAR is based on GAMMA SAR interferometric processing software (Werner et al., 2000; Wegmüller et al., 2016) and employs a spectral diversity method to co-register the Sentinel-1 Single Look Complex (SLC) acquisitions (Scheiber and Moreira, 2000) to generate Resampled SLC (RSLC) data and create interferometric products. The phase of each interferogram is unwrapped using the statistical-cost algorithm SNAPHU (Chen and Zebker, 2002; Hooper, 2009) and then these interferograms are multilooked, with a factor of 4 looks in azimuth and 20 looks in range. We tested two global Digital Elevation Model (DEM) data sets to remove topographic phase contributions and for geocoding; a) NASA's Shuttle Radar Topography Mission (SRTM) 1-arc and 30 m horizontal resolution in C-Band and X-Band worldwide (Farr et al., 2007), open access data for manycountries since August 2015 (Figure Supplementary S1b); and b) Copernicus DEM, which was accessible since 2021, based on the radar satellite data acquired during the TanDEM-X mission with 30 m resolution (European Space Agency, 2021) (Figure Supplementary S1a). We use two LiCSAR frames (ID 018A_09253_131313 and 142D_09148_131313, ascending and descending respectively, Fig. 2) that cover the Sangay volcano area in the period between 2014 and 2022 at sampling intervals of 6 (since 2017) and 12 (2014–2016) days. We created short and longer interferograms, with time intervals every 6, 12, 24 days and 1 month for every acquisition and also 2, 3, 6, 9 months and 1 year in between. In total, 2546 and 1711 interferograms constructed from 264 and 265 acquisitions were used for the ascending and descending tracks respectively.

2.2. Time series processing

We constructed time series of phase using a small baseline subset (SBAS) approach to generate average velocities and cumulative line-of-sight displacements (LiCSBAS (v1.5.11), Morishita et al., (2020); Morishita, (2021)). Due to high phase decorrelation associated with amazonian rainforests, we are limited in our analysis to an area of ~60 km^2 around the Sangay Volcano where there are areas of exposed rock and where forest cover is patchier.

We assess the quality of our unwrapping by identifying and removing bad interferograms from the network used for time series inversion. Initially, we employ threshold statistics, including the average coherence and coverage of the unwrapping data. We select a threshold of 0.3 for unwrapping data quality (the threshold determines the minimum acceptable coverage of valid unwrapped pixels of interferograms) and 0.05 for average coherence (e.g. interferograms may contain inconsistent and decorrelated information caused by factors such as vegetation or snow cover). Interferograms below this threshold will be excluded from further analysis. We apply a phase closure technique (e.g. Biggs et al. (2007)) to identify and remove interferograms with unwrapping errors. We estimate the most appropriate thresholds (Supplementary Table S1) for loop closure error and root mean squared residual in velocity (rms) by plotting them against each other and defining an area where most of the points are concentrated (Supplementary Fig. S2, after Watson et al. (2022), Supplementary Table S2). We use the better interferograms according to these metrics with the small baseline inversion (Morishita et al., 2020), similar to the NSBAS approach (Doin et al., 2011) to construct the timeseries. We estimate the velocity and standard deviation (STD) using a bootstrap method and use spatio–temporal consistency (STC) (Hanssen et al., 2008) as an additional measure of uncertainty on the velocities. We assess the impact of our selection of

thresholds for loop error (a proxy for number of unwrapping errors) by comparing the velocity maps for thresholds of 0, 25 and 200 and find that the spatial pattern and time series trend are consistent across all values, although when no unwrapping errors are permitted, coverage is lost closest to the volcano's summit (Supplementary Fig. S3).

We tested the effectiveness of correction for atmosphere using Generic Atmospheric Correction Online Service (GACOS) (Yu et al., 2018) (Supplementary Methods Appendix A.2), which uses European Centre for Medium-Range Weather Forecasts (ECMWF) data to predict atmospheric phase delays. We found that the quality of interferograms as assessed by phase standard deviation was degraded by this correction, perhaps due to the impact of steep topography on local water vapour and hydrostatic pressure, as well as the low volume of ECMWF inputs in the area (e.g., Dogru et al. (2023)). The impact of seasonal contributions to phase was therefore mitigated using spatiotemporal filtering (Hooper et al., 2012) with a temporal window width of 18 days and a spatial width of 1 km (iterative testing of filtering approaches shown in Supplementary Fig. S4). We further applied a linear elevation-phase correction to subtract the topography-correlated component of atmospheric signals (e.g., Morishita et al. (2020)). Finally, we investigated the impact of the choice of reference pixel location using the method proposed by Yip et al. (2019) and selecting a reference area of dimension 100 × 100 m and centered on (−78.3168°, −1.9938°) (Supplementary Methods Appendix A.3).

2.3. The impact of network design

Due to high rates of temporal decorrelation, our initial strategy at Sangay was to construct time series from short temporal baseline (6 or 12 day) interferograms. However, we find that this introduces systematic effects into our time series, consistent with the 'fading signal' described by Ansari et al. (2020) and demonstrably related to land cover type and vegetation characteristics (Maghsoudi et al., 2021; Purcell et al., 2022). To determine the best possible network for analysing deformation at Sangay, we construct time series for different combinations of interferograms with durations ranging from 6 to >100 days (e.g., Purcell et al. (2022)), (Figure Supplementary S5). Time series constructed from networks of only short timespan interferograms (Fig. 3a,b) show spurious apparent uplift rates exceeding 5 cm/yr. We found that incorporating interferograms spanning >30 days reduced this effect (e.g., increasing Gaussian phase distributions shown in Figure Supplementary S5), especially with the removal of those with shorter timespans (e.g., <12 days, Fig. 3 e,f).

The shift to using a network incorporating longer timespan interferograms (> 30 days) results in a smaller coherent area around Sangay's summit, and data coverage loss in the North, East and South. However, the apparent phase gradient between the rockier, upper flanks of the volcano and the more densely vegetated lower flanks is significantly reduced by this strategy, with systematic tests showing a clear relationship between the timespans of the interferograms used in the network and apparent phase gradient in the time series (Fig. 3 g).

As there are no GNSS stations located on Sangay, we cannot ground-truth our InSAR time series locally. We therefore compare the time seriesconstructed from a range of possible interferogram networks with the deformation values measured at the locations of permanent GNSS stations elsewhere in the same Sentinel-1 frame (at Bilbao and Riobamba see location in the supplementary Fig. S6). These show that reducing our analysis to only interferograms spanning ≥12 days was sufficient to bring the InSAR time series in line with the GNSS.

2.4. Analysis of displacement signals

We estimate the East-West and vertical components of motion from both ascending and descending maps of cumulative displacement (November 2015 and July 2022) (Fig. 4, Figure Supplementary S7), based on the assumption that north-south displacements make a negligible contribution to the satellite line-of-sight (Wright et al., 2004; Motagh et al., 2017). While this assumption is imperfect, we favour this to the alternative assumption of radially symmetric deformation given the spatial complexity of the line of sight signals.

The displacement patterns at Sangay are spatially and temporally complex, and suggestive of multiple active deformation sources. We

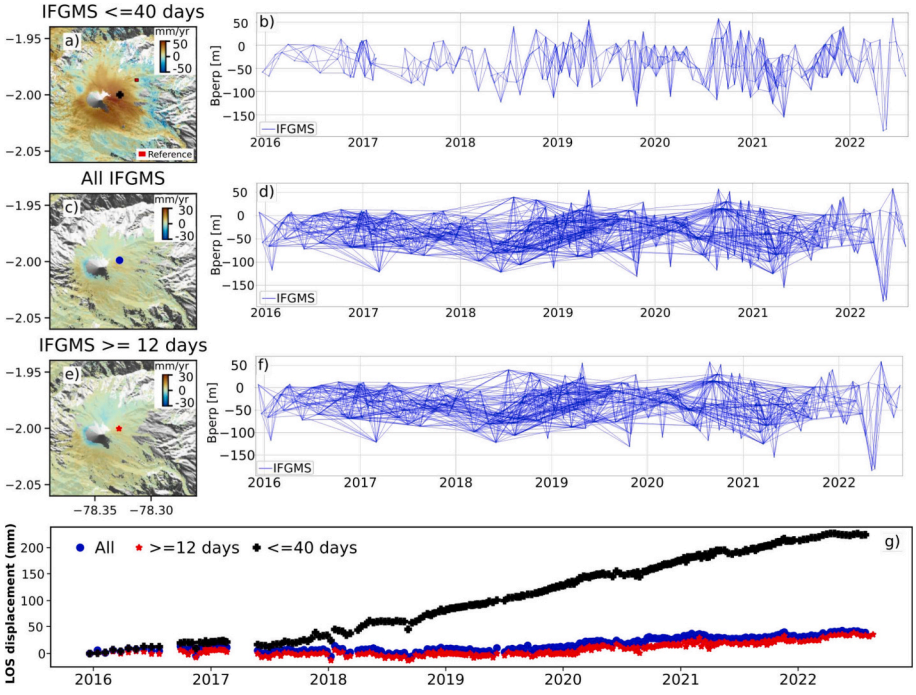

Fig. 3. Illustration of velocities derived from descending data for networks incorporating different combinations of shorter and longer interferograms (IFGMS): a), b) ≤ 40 days; c), d) All interferograms (shorter and longest); e), f) ≥ 12 days. g) Time series demonstrate the impact of interferogram network design (point marked on panels a, c and e).

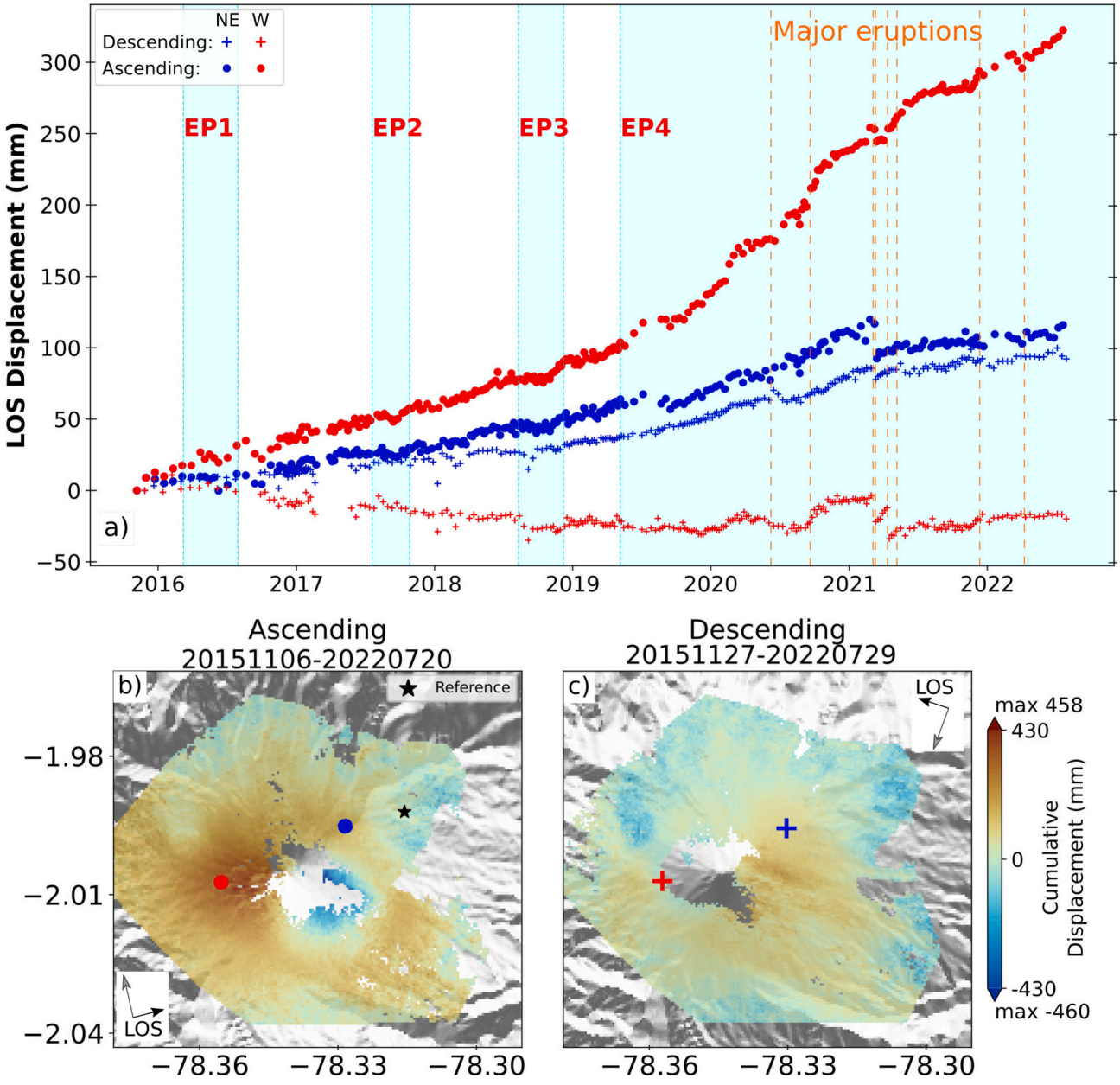

Fig. 4. a) LOS displacement time series for related pixels around the volcano edifice for the whole period (between 2016 and 2022) of W (−2.023°, −78.338°) and NE (−1.996°, −78.327°) pixels to the reference (−1.993°, −78.316° black star). The cyan colour in a) represents eruptive periods (EP) defined by Vásconez et al. (2022). Orange dashes lines represent the major eruptions since 2019 recorded and reported by the IG-EPN and Hidalgo et al. (2022). b) Ascending and c) Descending cumulative displacement maps. (For interpretation of the references to colour in this figure legend, the reader is referred to the web version of this article.)

therefore use Independent Component Analysis (ICA) (Hyvärinen et al., 2004) to decompose cumulative displacements into linear, additive components that maximise the independence of their spatial patterns (Ebmeier, 2016; Gaddes et al., 2018; Maubant et al., 2020). This is based on the assumption that spatial components at Sangay have a non-Gaussian distribution, so as more components are added together the mixed signal becomes increasingly Gaussian.

We apply spatial ICA to decompose cumulative displacements at Sangay between 2019 and 2022 using the application of the FastICA algorithm (Hyvärinen et al., 2004) using multiple restarts and bootstrapping implemented by Gaddes et al. (2019). We iteratively select the number of independent spatial components to be retrieved (e.g., Ebmeier (2016); Purcell et al. (2022)), and find consistent results for 7 from the ascending data and 11 from the descending data. Over 200 repeats for each dataset the independent components retrieved remained similar, implying that the data represents a significant property of the input dataset (e.g Purcell et al. (2022)). However, a small amount of 'ghosting' (mixing of independent signals between components) remains.

2.5. Modelling deformation

The location, volume change, and shape of the magma body causing deformation in volcanoes can be investigated using analytical or numerical models that describe the relationship between a volume change in the Earth's crust and the displacement of the Earth's surface. This can be achieved using inversion tools that utilize simple analytical elastic half-space models, such as Geodetic Bayesian Inversion Software (GBIS) (Bagnardi and Hooper, 2018), or numerical models that employ a finite or boundary element approach to account for inelastic rheologies,

varying crustal structure, and topography (e.g., Hickey et al. (2020); Fukushima (2005); Cayol et al. (2020a)).

The incorporation of realistic topography is critical for modelling displacements at Sangay, due to its 2 km of relief from base to summit and slope angles exceeding 30°. Neglecting topography can result in overestimations of overpressure (or opening), source length/width, volume and poor constraints on depth (Cayol and Cornet, 1998; Fialko et al., 2001; Fukushima, 2005). We therefore use a 3D Boundary Element Method (BEM) to model elastic displacements, called 'DefVolc' (Cayol and Cornet, 1997; Fukushima, 2005; Cayol et al., 2020b; Shreve et al., 2022). This allows us to incorporates Sangay's real topography from the Copernicus 30 m DEM, represented by a mesh (resolution 260 m) of radius 2400 m inside a courser mesh that extends out to 19,000 m. Our topographic mesh comprised 53 mesh nodes and 124 mesh elements (FigureSupplementary S8a).

We performed an inversion of our InSAR data to find the best fit parameters for a range of geodetic source geometries including ellipsoid, planar ellipsoid, spherical and quadrangle shapes (Fukushima, 2005; Fukushima et al., 2010; Cayol et al., 2020a). Our inversion uses near-neighborhood optimization algorithms and accounts for correlated noise in the interferometric phase using data covariance (Fukushima, 2005). We downsampled our InSAR data for inversions with a regular spacing interval of 260 m for both tracks (617 points Figure Supplementary S8b). Correlation distances (a_c) and phase variance (σ^2) for each track were $\sigma^2 = 1.45 \times 10^3$ mm^2, $a_c = 7.34 \times 10^5$ mm for ascending and $\sigma^2 = 1.8 \times 10^3$ mm^2, $a_c = 1 \times 10^6$ mm for descending (following noise analysis of Fukushima (2005)). We used a Young's modulus of 5 GPa and Poisson's ratio of 0.25 (e.g. Fukushima (2005)). We find that varying the Young's modulus and Poisson's ratio has a minimal effect on our solutions (see Supplementary Table S3).

For the first iteration, parameter size is explored by computing forward models (e.g 546 forward models for Quadrangle) with random combinations of the estimated model parameters (Supplementary Table S4). Subsequent iterations of 50 models were then made to search for the parameters with the lowest misfit from the previous iteration (Fukushima, 2005). The iteration ended when the standard deviation of the misfit values from the last forward calculation was less than the threshold criterion $\sigma = 0.3$ (e.g. Shreve et al. (2022)).

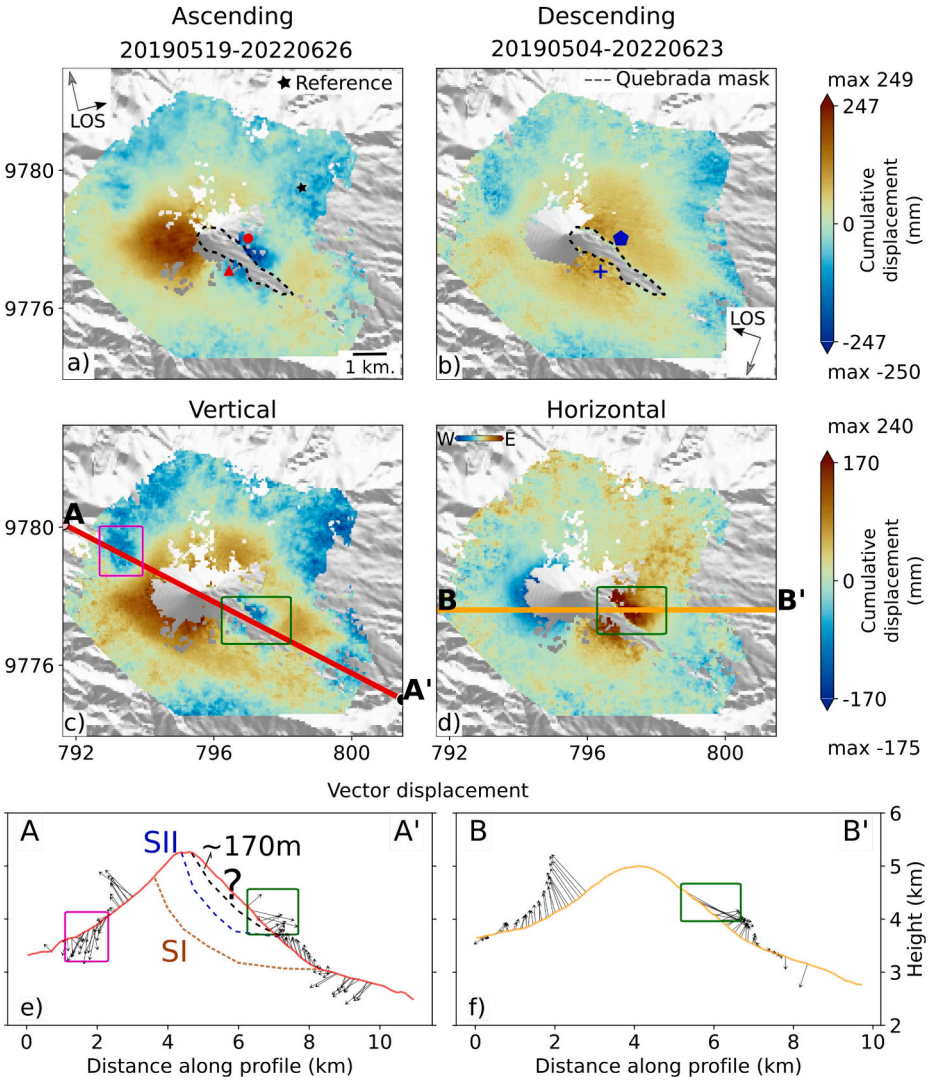

Fig. 5. Sangay volcano cumulative displacement maps for the period between 2019 and 2022 that correspond to the last explosive activity. (a) Ascending, (b) Descending tracks. Components of motion: (c) Vertical and (d) Horizontal (East-West)and show two line profiles B–B′ (east-west, orange) and A–A' (northeast-southwest, red); (e, f) correspond to the motion as vectors displacement through Sangay Volcano for each profile. Green and purple boxes represents the areas, which we have referred to as "Landslide/Quebrada", furthermore, in e), the scars of the two avalanches recorded on the volcano are depicted: Scar Sangay I (brown dashed lines, SI) and Scar Sangay II (blue dashed lines, SII). In d) horizontal displacement red indicates eastern motion. (For interpretation of the references to colour in this figure legend, the reader is referred to the web version of this article.)

3. Results

Our InSAR measurements of displacements at Sangay show spatially and temporally complex patterns (Fig. 4, Fig. 5, Figure Supplementary S11 and S12) and comprise (1) multi-year LOS range decrease (uplift) on the western and northeastern flanks, (2) transient pauses or episodes of range increase (subsidence) during explosive episodes and (3) a persistent range increase (subsidence) in ascending imagery on the southeastern flank of Sangay aligned with a young quebrada (steep, erosional valley).

Decomposition using spatial ICA consistently results in four components identifiable from their spatial or temporal patterns (Fig. 6). Two of these components can be related to either transition magmatic activity or specific explosions (Fig. 6 a,b,d,e), while two relate to processes limited to the new quebrada in the SE (Fig. 6 g,h,j,k).

3.1. Long-term uplift

The dominant trend in Sangay's deformation between late 2015 and 2022 is uplift, with highest rates on the western flank of the volcano in the ascending data. Decomposition of the two lines of sight into vertical and East-West components show that motion is primarily upwards, with westward displacement on Sangay's western flank (Figure Supplementary S7). In 2019, there was a notable increase in the displacement rate, with the ascending LOS rate on the western flank more than doubling compared to previous years. This change reflects not only differences between the eastern and western flanks but also variations within the same flank over time, both before and after 2019 (Fig. 4a). This change coincided with the transitional period in 2018–19 identified by Herrería (2020) and Andrade (2021), when Sangay shifted from effusive activity dominated by gas plumes with low ash content, dome activity and lava flows (2015–2019) to a most intense and more explosive period of eruption from 2019 onwards ('EP4', on Fig. 4), characterized by explosions with a high ash content, lava fountaining, lava flows and associated pyroclastic currents and secondary lahars. It is noteworthy that the rate of uplift was higher during the period 2019–2022, despite the occurrence of more frequent high ash plumes and lava flows, in contrast to earlier episodes 'EP1–3' (as defined by Vásconez et al., (2022)), during which displacements temporarily ceased (Fig. 4a).

The pattern of this persistent uplift is consistently retrieved as an independent spatial component (Fig. 6a), and time series reconstructed using the appropriate mixing matrix rows show a steady rate from early 2020 onwards. It therefore seems that the same geodetic source is likely to be causing this uplift for the whole time period. Our measurements are limited to the upper flanks of Sangay (elevations over 3500 m) due to poor coherence on the vegetated lower slopes. This means that we are limited to observing displacements caused by relatively shallow sources. However, vertical displacements are actually limited to a zone within 1.5 km of the volcano summit (Fig. 5), so the magmatic zone responsible for this uplift must itself be limited to relatively high within the volcano's edifice.

3.2. Major explosions and transient displacements

We show the timings of the the large explosions described by Vásconez et al. (2022); Hidalgo et al. (2022) and Bernard et al. (2022) as orange lines on Fig. 4 and Figure Supplementary S9. Interferograms spanning these events have some coherence loss around Sangay's summit, and have no distinct displacement patterns distinguishable above atmospheric noise. However, there are clear changes in displacement rate and sometimes reversals in displacement direction during events on 19.09.2020, 07.05.2021, 12.12.2021 and 04.04.2022. Only the biggest of the major explosions on 11.03.2021 is reliably captured as a separate spatial component by the ICA. This event caused sudden range increases (subsidence) in both ascending and descending time series at the time of eruption onset (Figs. 4 and 6). Both increased SO_2 emissions and elevated seismicity have been measured in the days preceding large explosions (Bernard et al., 2022). For example, TROPOMI measurements showed SO_2 emissions exceeding 1000 tons for three days before a major explosion on 19th September 2020, while the number of earthquakes increased for about a month before the eruption. We lack the temporal sampling to be sure of whether displacement rates changed in the three days before this explosion, but can see that there was no change in displacement rate above the level of noise in our data over the month before.

3.3. Flow subsidence and down-slope movement

Sangay's exceptionally high levels of activity have resulted in the formation of large erosional quebradas (e.g., Gallant et al. (2020)) filled with tephras and pyroclastic deposits (Volcanes del Ecuador, 2020). The most recently formed quebrada runs to the southeast (Herrería, 2020; Vásconez et al., 2022; Hidalgo et al., 2022), and is at the centre of a patch of subsidence in our ascending imagery (Fig. 5a). We are confident that this patch of subsidence relates to a shallow process linked to young deposits because (1) it is limited in extent to the area surrounding the location of major pyroclastic flow deposits in 2018, 2019, 2020, 2021 and (2) the direction of displacements is downslope (see profiles on Fig. 5e and time series in Figure Supplementary S20).

Flows have travelled down the southeastern quebrada since at least the 1890s (e.g., Fig. 7h), leading to periods of topographic growth (e.g., DEM difference between 2000 and 2011–2015, Fig. 7e and Figure Supplementary S1) and loss, for example during the lava front collapse on June 6, 2020. Subsidence in this area is split into two components by the spatial ICA. One of these has the same shape as some of the most recent deposits and shows steady displacement rate (e.g., Fig. 7a and c, d). We attribute this to a compaction process within the flow deposits themselves (e.g., Wittmann et al. (2017)). The other component (Fig. 7b) spans the quebrada and its limits can be seen as sharp phase boundaries in some individual interferograms (Fig. 7f). It is therefore more consistent with a mass wasting (e.g., Schaefer et al. (2019)) than a loading mechanism (Pinel et al., 2022). There are some variations between downward displacement time series on either side of the valley, suggesting that the down-slope motion is more likely to the result of multiple units sliding in a similar manner (e.g. Ebmeier et al. (2014)) rather than the slip of a single unit several hundred metres across.

4. Magmatic deformation sources

We prepare our data for modelling by first masking out zones of flow subsidence and down-slope displacements identified from a combination of optical imagery (Planet Explorer Optical, 25.08.2020, 28.06.2002 (Planet Team, 2017) and Sentinel 2 15.06.2022 (ESA Team, 2015)), X-band radar (TerraSAR-X, 03.03.2020) and a DEM created by IG- EPN from aerial photos spanning the upper SE part of the volcano (Fig. 7 and Figure Supplementary S10). Since the uplift-related displacement pattern seems to have been consistent since 2019, we use cumulative displacements between 2019 and 2022 for our inverse modelling.

We explore four different potential geodetic source geometries to account for the long-term uplift at Sangay: an ellipsoid (9 geometrical parameters), a planar ellipsoidal shape (8 geometrical parameters), a spherical source (3 geometrical parameters) and a quadrangle (up to 12 geometrical parameters) (Fukushima et al., 2010; Cayol et al., 2020a). We restrict the source depth to lie within the volcanic edifice. Supplementary Tables S4, S5 and S7 describe all parameters tested, their range of acceptable values and provide the best results for each geometry. We assess the performance of each model (Table 1) using four metrics: (1) the percentage of the data explained (Fukushima et al., 2010), (2) the root-mean-square (RMS) error (mm) (Wauthier et al., 2012), (3) the

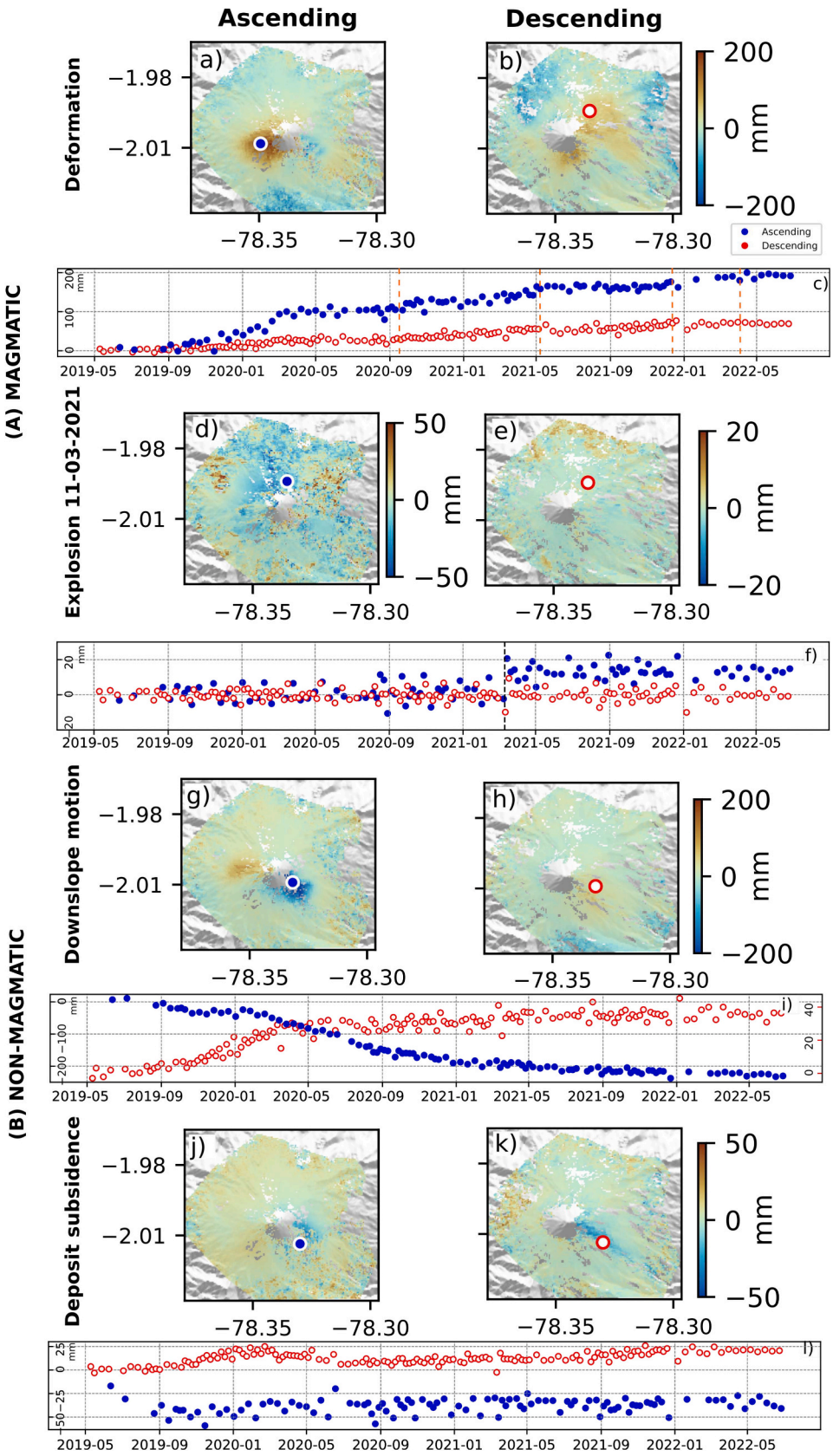

Fig. 6. Results of Independent Component Analysis (ICA) for both tracks showing the reconstruction of components and the time series for: (A) Magmatic activity: in a, b, c) Magmatic deformation; d, e, f) Component of the March 11, 2021 explosion and (B) Activity related to non-magmatic sources: g, h, i) Downslope motion; j, k, l) Deformation in deposit subsidence. The extracted points for time series for each components are shown in each reconstructed IC in blue (ascending) and red (descending). Orange dashes lines in a) represent the major eruptions since 2019 recorded and reported by the IG-EPN and Hidalgo et al. (2022). (For interpretation of the references to colour in this figure legend, the reader is referred to the web version of this article.)

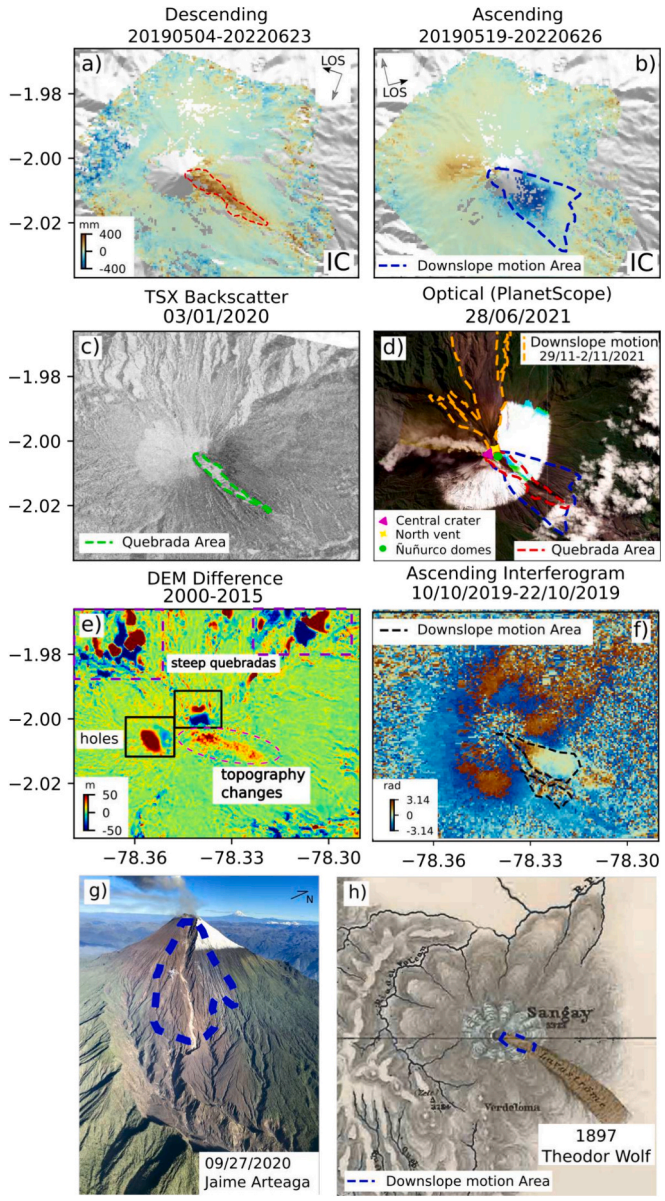

Fig. 7. Deformation related to the deposition and quebrada observed in the independent components in a) Descending; b) Ascending respectively; c) The Terrasar–X data amplitude image of January 03, 2020, shows the shape of the quebrada with green dashed lines; d) Optical images from Planet Explorer, taken on August 25, 2020, depict the shapes of the deposits and quebrada, e) The difference between Copernicus (2011–2015) and SRTM DEM (2000) is shown; f) The ascending interferogram displays deformation patterns in the southeast area; g) The southeast flank of Sangay volcano displays the new quebrada formed during the eruptive period since May 2019 (Photo dated 09/27/2020; courtesy: Jaime Arteaga, taken from Volcanes del Ecuador (2020)). The approximate area is outlined with blue dashed lines, corresponding to the independent area based on DEM, photos, and interferograms; h) The map of Sangay volcano drawn by Theodor Wolf in Alphons Stübel's book "Das Vulkangebiet von Ecuador" (1897) is taken from Volcanes del Ecuador (2020). The locations of the central vent, Ñuñurco dome and north vent are shown in panel d. (For interpretation of the references to colour in this figure legend, the reader is referred to the web version of this article.)

weighted Chi-square (χ^2) (e.g. Lin et al. (2010)), which accounts for the number free parameters required to characterise each geometry (Supplementary table S8) and finally 4) the Akaike Information Criterion (AIC, Akaike (1974)), which enables us to select models based on their relative values with different numbers of model parameters. The most probable model is characterized by the lowest AIC (e.g. Fukushima et al., 2010; Wauthier et al., 2012) (Supplementary table S6).

We find that only vertically extensive sources located within the western part of Sangay's edifice can account for the observed displacement patterns (Figure Supplementary S13). In particular, the westward component of motion clear in the ascending imagery on the western flank of Sangay requires the presence of a shallow source, opening in a slope orthogonal direction. Of the sources we test, both a shallow, inclined vertically extensive ellipsoid and a more plausible westward dipping quadrangle capture the main features of this displacement pattern.

Our preferred solution entails an inclined quadrangular plane, with a westward dip, situated on the western flank of the edifice. This plane extends from just beneath the southwest flank near the crater to a depth of approximately 4.2 km above sea level (Figs. 9 and 8). The estimated volume increase 2019–2022 is 1.1 × 10^6 m^3. For this source, the one-dimensional posterior probability density functions (PPDs) for the diagonals are quasi-symmetric, exhibiting a single peak (Figure Supplementary S14), and distributions close to Gaussian. The two-dimensional PPDs for the off-diagonals display negligible trade-offs. However, while the fit to the data is reasonable, we are cautious about the extent to which this geometry captures magmatic structures at Sangay. We note that our data are noisy, and that poor coherence effectively limits measurements to displacements originating within the edifice and this is a non-unique solution. The aspects of our modelling results that we consider to be required by the data and therefore interpretable are: (1) that the source (or group of sources) is vertically extensive and extends from close to the volcano's summit down to the base of the edifice, (2) that co-eruptive intrusion is taking place into the western flank of the volcano.

4.1. Temporal evolution of source volume

Firstly, we identify the optimal quadrangle geometry for the full cumulative deformation between 2019 and 2022, which has a maximum value of 249 mm and comfortably exceeds the magnitude of noise in the time series. We then fix the source location, and solve for cumulative displacements over shorter, noisier, time intervals as shown in Fig. 10. This required the assumption of that the source location is constant, but makes our estimation of volume less sensitive to noise in each time interval (e.g Reddin et al. (2023)):(1) seven six-month intervals and (2) ten intervals of different duration that separated out major explosions (Supplementary Table S10). We allow variations in the parameters Strike, Dip, Length and Bottom Length. We find that the magma source volume increased linearly with time (e.g., intrusion rate was constant, Fig. 10). Only during the eruptive events of March and December 2021 was there transient volume loss.

5. Discussion

5.1. Magmatic structures at Sangay

The only geometries that could account for the long-term co-eruptive uplift at Sangay are located beneath its western flank, and extend vertically down through its edifice, dipping to the west. Our preferred geodetic source solution (westward dipping quadrangle, Figs. 9 and 8) describes a gradually opening dyke-like pathway extending through the entire height of the edifice. While the addition of another, sub-edifice source reduces our residuals (Figure Supplementary S15) and the value of AIC (Supplementary table S6), we lack the data coverage on Sangay's lower flanks to constrain the characteristics of any sub-edifice reservoir. We therefore limit our discussion to magmatic structures within Sangay's edifice.

Sangay exhibits both characteristic 'open' and 'closed' behavior (Chaussard et al., 2013; Reath et al., 2019, 2020) and is unusual in that this occurs simultaneously from different vents. The conduit supplying

Table 1
Our best solutions for multiple source geometries. A full list of geometric parameters are shown in Supplementary Table S4. Comparison of main parameters from different Lat and Lon represent the location in surface for each source. Furthermore, we evaluate the performance of each model and present three metrics:(1) the percentage of the data explained (Fukushima et al. (2010)), (2) the root-mean-square (RMS) error (mm) (Wauthier et al. (2012)) and finally (3) the weighted Chi-square (χ^2) (e.g. Lin et al. (2010).

Geometry	Latitude	Longitude	Depth (km)	Volume change (m^3)	Ascending			Descending		
					RMS (mm)	% Data Explained	χ^2	RMS (mm)	% Data Explained	χ^2
Sphere	−2.005	−78.344	3.5	1.0×10^6	39.4	33.2	7.2	32.5	14.2	7.4
Shallow Ellipsoid	−2.006	−78.34	3.2	1.8×10^6	34.8	42.9	1.8	35.1	8.0	6.4
Shallow Quadrangle	−2.002	−78.342	4.9	1.1×10^6	32.9	44.3	2.7	38.7	−3.5	15.6
Planar Ellipsoid	−2.0002	−78.342	2.0	2.8×10^6	39.2	38.8	3.4	26.2	40.3	3.4
Quadrangle	−1.99	−78.344	2.2	2.4×10^6	40.7	34.7	5.0	27.6	36	3.6
Ellipsoid	−2.0001	−78.342	2.2	2.6×10^6	39.3	38.9	3.3	26.4	40.7	2.9

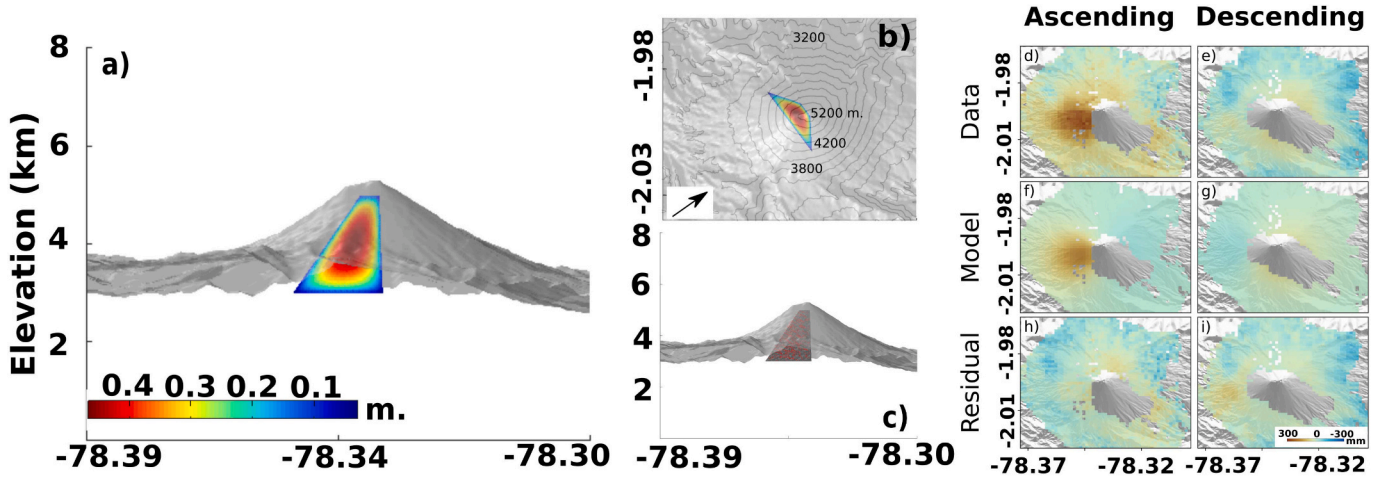

Fig. 8. Volume opening representation for shallow quadrangle (a) view from southwest (arrow view in figure b); (b) in plan view (North-South) and (c) upper surface displacement. Comparison between (d,e) Observed line-of-sight (LOS) displacement, Model corresponding to the best quadrangle (preferred solution) (f,g) and (h,i) Residual for Descending and Ascending between 2019 and 2022.

the Ñuñurco domes seems to remain open (Vásconez et al., 2022; Hidalgo et al., 2022), producing constant degassing and the effusion of new lavas. The central crater is the site of explosive eruptions and ballistics, sealing off between eruptions. A new crater to the north of the Ñuñurco domes also opened in December 2021 and produced a lava flow, which then collapsed to the north (Fig. 7d). Given that the eruption sites are so close (within 300 m), they are likely to be supplied from the same magma pathways up to shallow depths. All lava effusion, and the majority of explosions at Sangay, take place without accompanying co-eruptive subsidence, and without causing excursions in the trend of long-term uplift. This suggests that magma flux into the edifice marginally exceeds the rate of eruption achievable through the 'open' conduit to the Ñuñurco domes, resulting in periodic opening of the central crater in a minor explosive eruption. These explosions are generally not sufficient to relieve the pressure in the feeder-dyke, which continues to open steadily throughout the eruption, causing persistent uplift. This is consistent with a continuous inflow of magma into the edifice (Vásconez et al., 2022) (Fig. 10) and volatile ascent to shallower levels (e.g. Champenois et al. (2014); Reverso et al. (2014); Hautmann et al. (2017)). The significant exception to this is the transient changes in displacement rate accompanying the two major explosions on the 5th and 11th March 2021 (Fig. 6 d,e,f), which were characterized by an increase in SO_2 emissions (Figure Supplementary S19d), continuous ash plumes (approximately 15 km above sea level), and major lava flows (IG-EPN, 2021).

Between 2019 and 2022 Sangay was in a steady state of both eruption, and intrusion into the edifice. By 2022, the uplift rate seems to have decreased slightly, until June 2022, end of the period under scrutiny in this investigation. During this period, both the central vent and the old western vent, characterized by explosive activity (ash emission accompanied by blocks on the flanks), were active. Degassing levels consistently remained above 500 tons on average between October 2021 and April 2022 (IGEPN, 2022). Notably, two peaks in outgassing (Figure Supplementary S19) were observed on March 15 and 30, 2022, potentially linked to a shift in deformation trend (see Fig. 4), and these peaks correlate with the eruptive activity recorded on April 4–6, 2022.

5.2. *Deposit subsidence and flank stability*

Sangay's historical eruptions have carved deep erosional valleys into its flanks, for example, the SE flank in 1897 (see Fig. 7h) or the northern sector in 1956 (Volcanes del Ecuador, 2020). These deep quebradas have been filled with fresh volcanic material during subsequent eruptions, making them prone to gravitational surface movements. Current deformation on the southeast flank of Sangay can be separated into components related to deposit compaction and alteration within the channel structure itself (Fig. 6j, k, l) and a broader displacement pattern that extends onto older deposits (Fig. 6g, h, i).

There are two significant hazard implications of the poorly consolidated deposits in this area. Firstly, loose deposits are channeled towards the lower part of the Volcan River (Fig. 2b) providing material for the generation of lahars. These threaten populated areas and important infrastructure in the Amazon region, especially after heavy rainfall (Bernard et al., 2022). Secondly, the combination of its very steep slope and long-standing flank motions (previously observed by Morales et al. (2016), 2007–2011) may indicate a susceptibility to the generation of major landslides. Valverde et al. (2021) modeled the type of collapse that would potentially impact the southeastern and eastern zone of the

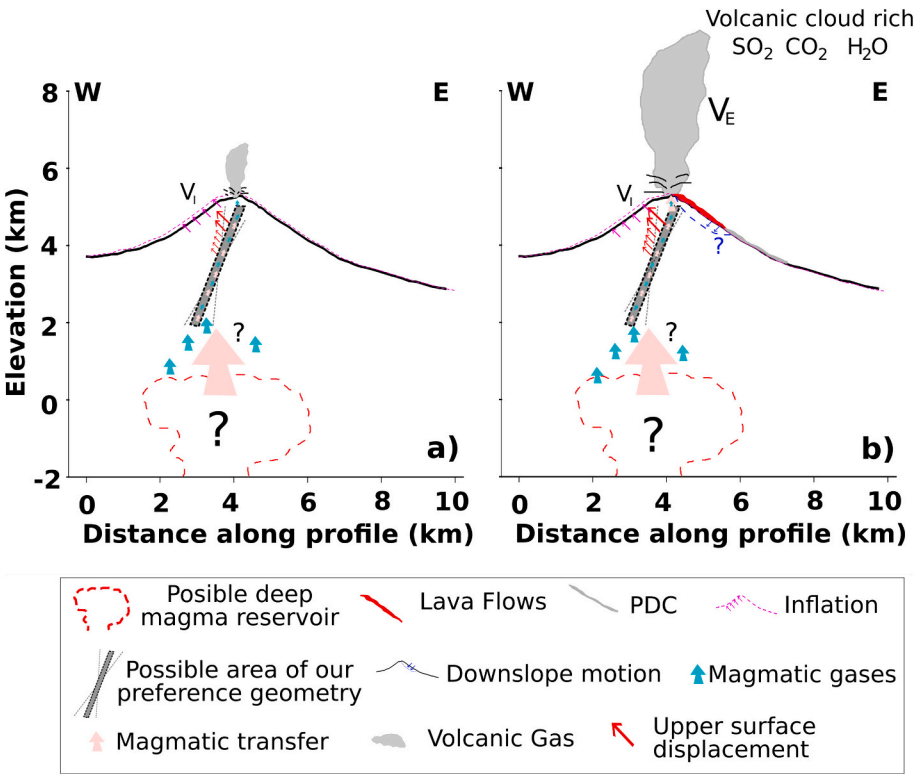

Fig. 9. Schematic diagrams illustrating the Magmatic System within the Volcano: (a) Between major explosions; (b) During eruption. Depicting an open dyke-like pathway extending throughout the entire height of the edifice, showcasing a consistent intrusion of magma over a period of at least four years of eruption.

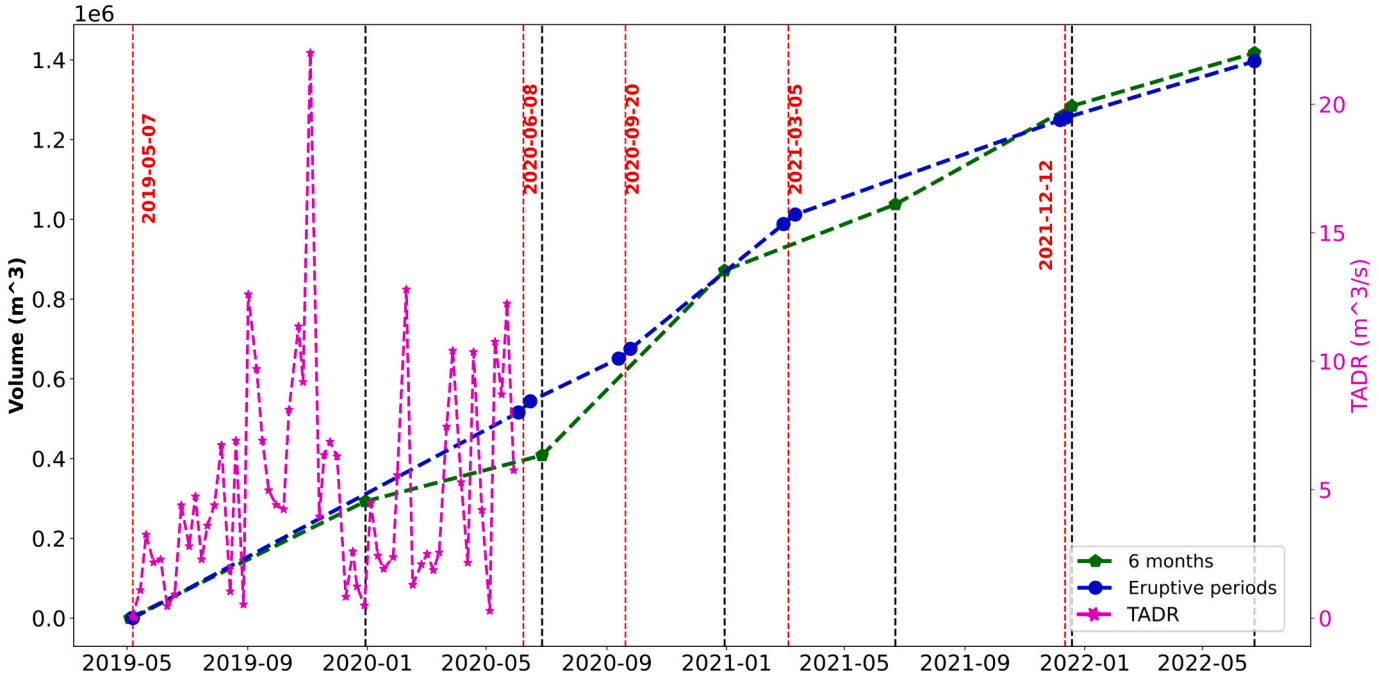

Fig. 10. Estimated magma volume changes as a function of time derived from InSAR source modelling. Green dashed lines represent the division every 6 months windows (black dashed vertical lines) and blue dashed lines show the division according important co-eruptive events (red dashed vertical lines). The magenta line represents the time-averaged discharge rate (TADR) in m^3/s estimated by Vásconez et al. (2022) between 2019 and 2020. (For interpretation of the references to colour in this figure legend, the reader is referred to the web version of this article.)

volcano. The model considered a "small volume scenario" of 4.3 km^3 (represented by the green shaded line in Fig. 5e). The volume of sliding material that we currently observed is only 20% of this, 0.85 km^3, as estimated from an area of 5 km^2 identified in section 3.3, with a minimum depth of 170 m estimated from the IG-EPN DEM. Our measurements show that displacements within this area are variable, suggesting that it is not a continuous unit. However this section of the edifice may be more vulnerable to gravitational failure, especially if

triggered by earthquake shaking.

5.3. Endogenous growth

The growth of a volcanic edifice occurs both externally due to the repeated deposition of fresh lavas and explosive products (exogenous) and internally (endogenous) due to the intrusion of magma (e.g. Biggs et al. (2010); Xu et al. (2017); Coppola et al. (2019); Mania et al. (2019); Dumont et al. (2024)). Our observation shows the endogenous growth of the Sangay stratovolcano due to the steady intrusion of magma during at least four years of eruption. Unlike previous observations of co-eruptive intrusion at Tungurahua (Biggs et al., 2010; Muller et al., 2018), at Sangay, magma seems to add into the edifice steadily, and was not associated with a particular eruptive event. Co-eruptive intrusion has rarely been reported at stratovolcanoes, perhaps due to challenges of making displacement measurements on steep topography, near active vents (e.g., Pinel et al. (2011)). However, high fluxes of thermal energy and gases at some systems have been interpreted as evidence of the endogenous growth at unknown depth within the magmatic zone (Francis et al., 1993).

The volume increase during 2019–2022 estimated from our preferred geometry of an inclined quadrangle is 1.1×10^6 m^3. For context, we estimate that the volume lost from the deepening of the southeastern quebrada to be 5.1×10^8 m^3. This estimate is based on the area of newly eroded parts quebrada from optical and backscatter images ($\sim 2.5 \times 106$ m^2) along with an average depth increase of 200 m. Lavas and pyroclastic flows during these years flowed down established channels away from the central edifice. They did not contribute to edifice growth, so it seems that the net mass balance for Sangay's edifice between 2019 and 2022 was negative. A relatively small proportion of the magma ascending through Sangay seems to remain in the edifice. Our volume calculations based on the deformation from 2019 to 2022 (1.1×10^6 m^3) is lower than the extruded lava volume of 172 ± 86 million m^3 estimated up to May 31, 2020 by Vásconez et al. (2022), based on thermal energy radiated. It is also lower than the total volume of ash of 9.9 million m^3 during the period 2019–2020, estimated by Andrade (2021), based on data on ash fall layer thickness. Comparison to these values suggests that the proportion of the magma supplied to Sangay that remains in its upper edifice lies somewhere between 0.5 and 10%. However, our estimate of intrusive volume is likely to be low due to the high compressibility of dyke-type geometry and gas-rich magma (Rivalta and Segall, 2008; Kilbride et al., 2016; Yip et al., 2022). In contrast, the abundance of thermal radiation from un-erupted magma in an open system may lead to an overestimation of dense rock equivalent of erupted lavas, as described by Coppola et al. (2022).

Our observation of steady, but relatively low magnitude volume increase in part of Sangay's edifice shows that while magma was able to ascend into the edifice, constrictions or intermittent blockage of very shallow conduit structures is sufficient to prevent all of it being erupted. This suggests that magma flux from depth has remained relatively steady during Sangay's most recent period of eruption, with larger explosions triggered by the development of transient, localised overpressure in the complex shallow conduit system. An increase in magma flux could break this pattern by initiating a period of higher effusion rate or causing greater deformation of the edifice, with implications for slope stability. Monitoring the rate of volume changes within the edifice is critical for capturing trends in magma flux at Sangay, and at other persistently active, apparently 'open' volcanoes.

6. Conclusion

We have demonstrated that Volcan Sangay has uplifted persistently throughout current eruption (May 2019–June 2022) in spite of frequent explosions and effusive activity. This uplift is caused by the steady growth of a quadrangular magma pathway dipping to the west beneath the volcano's western flank. Only the largest explosions in this time period in March 2021 caused significant interruption to the long term displacement trend. Reliable InSAR measurements on Sangay's edifice required a network of interferograms that incorporated long timespan pairs and omitted shorter time spans to limit the impact of a fading signal. The separation of spatial displacements patterns into independent components shows at least four separate processes taking place at Sangay: (1) long term uplift with a rate of 64 mm/yr vertical between 2019 and 2022, (2) transient subsidence during major explosions in 2021, (3) the subsidence of fresh deposits and (4) the down- slope displacements on the volcano's southeastern flank. Our measurements show the usefulness of InSAR data for monitoring at Sangay in spite of an especially challenging setting, and set out a suitable processing and analysis strategy. Monitoring rates of endogenous growth at Sangay and other persistently active volcanoes is important for accurately capturing trends in magma supply. Even where the intrusive magma flux is relatively low, these subtle changes in magma supply can have significant implications for the stability of the volcano's edifice. Understanding these dynamics is essential for assessing volcanic hazards and mitigating risks to nearby populations and infrastructure.

CRediT authorship contribution statement

Pedro Alejandro Espín Bedón: Conceptualization, Formal analysis, Investigation, Writing – original draft, Visualization, Writing – review & editing, Formal analysis, Data curation. **Susanna K. Ebmeier:** Conceptualization, Funding acquisition, Methodology, Supervision, Writing – review & editing. **John R. Elliott:** Conceptualization, Funding acquisition, Methodology, Supervision, Writing – review & editing. **Tim J. Wright:** Conceptualization, Methodology, Supervision, Writing – review & editing. **Patricia Mothes:** Writing – review & editing, Supervision. **Valérie Cayol:** Methodology, Writing – review & editing, Supervision. **Yasser Maghsoudi:** Resources, Data curation. **Milan Lazecký:** Resources, Data curation. **Daniel Andrade:** Writing – review & editing, Supervision.

Declaration of competing interest

The authors declare that they have no known competing financial interests or personal relationships that could have appeared to influence the work reported in this paper.

Data availability

The Sentinel-1 InSAR data are copyrighted by the European Space Agency and provided freely through the Copernicus Open Access Hub. Sentinel-1 InSAR data are also freely distributed by the Alaska Satellite Facility (https://asf.alaska.edu/). Processed SAR images, coherence, wrapped interferograms, and unwrapped interferograms used in this work can be found on the COMET-LiCS Sentinel-1 InSAR portal (https://comet.nerc.ac.uk/COMET-LiCS-portal/). LiCBAS software package can be found at https://github.com/yumorishita/LiCSBAS (Morishita et al., 2020). The software for inverse modelling can be found at DefVolc web page (http://www.opgc.fr/defvolc/Vue/MainPage.php). ICASAR software package can be found at https://github.com/matthew-gaddes/ ICASAR (Gaddes et al., 2019).

Acknowledgments

This work was undertaken on ARC4, part of the High Performance Computing facilities at the University of Leeds, UK. LiCSAR contains modified Copernicus Sentinel data (2014- 2022) analyzed by COMET. LiCSAR uses JASMIN, the UK's collaborative data analysis environment (http://jasmin.ac.uk). PE is supported by the University of Leeds through International Funding and Research Council Funded. SKE is supported by a NERC Independent Research Fellowship (NE/R015546/1). John Elliott is supported by a Royal Society University Research

Fellowship (UF150282 & URF211006). COMET is the UK Natural Environment Research Council's Centre for the Observation and Modelling of Earthquakes, Volcanoes and Tectonics, a partnership between UK Universities and the British Geological Survey. Figures were produced using Python, Matlab and others based on the volcano practical (https://github.com/andwatson/volcano_practical). This is Laboratory of Excellence ClerVolc contribution number 659. We thank all the staff of the Instituto Geofisico Quito, Ecuador who have worked in the monitoring of Sangay Volcano activity as well as in the processing of data and field observations. We thank the two reviewers, Federico Galetto and Federico Di Traglia, whose comments helped to improve this article.

Appendix A. Supplementary data

Supplementary data to this article can be found online at https://doi.org/10.1016/j.jvolgeores.2024.108147.

References

Akaike, H., 1974. A new look at the statistical model identification. IEEE Trans. Autom. Control 19 (6), 716–723. https://doi.org/10.1109/TAC.1974.1100705.

Allard, P., 1997. Endogenous magma degassing and storage at Mount Etna. Geophys. Res. Lett. 24 (17), 2219–2222. https://doi.org/10.1029/97GL02101.

Alvarado, A., 2012. Néo-tectonique et cinématique de la déformation continentale en Équateur.

Amelung, F., Jonsson, S., Zebker, H., Segall, P., 1999. Prospects of Volcano Geodesy with ERS Radar Interferometry.

Andrade, I.J.F., 2021. Trabajo de titulación, modalidad Proyecto de investigación presentado como requisito previo a la obtención del título de Ingeniero en Geología (PhD thesis). Universidad Central. http://www.dspace.uce.edu.ec/handle/25000/26383?mode=full.

Ansari, H., Zan, F.D., Parizzi, A., 2020. Systematic Interferometric Phase Biases and their Impact on Earth Surface Deformation Monitoring.

Arnold, D., Biggs, J., Wadge, G., Mothes, P., 2018. Using satellite radar amplitude imaging for monitoring syn-eruptive changes in surface morphology at an ice-capped stratovolcano. Remote Sens. Environ. 209, 480–488. https://doi.org/10.1016/j.rse.2018.02.040.

Bagnardi, M., Hooper, A., 2018. Inversion of surface deformation data for rapid estimates of source parameters and uncertainties: a Bayesian approach. Geochem. Geophys. Geosyst. 19 (7), 2194–2211. https://doi.org/10.1029/2018GC007585.

Bathke, H., Shirzaei, M., Walter, T.R., 2011. Inflation and deflation at the steep-sided Llaima stratovolcano (Chile) detected by using InSAR: deformation modeling at Llaima volcano. Geophys. Res. Lett. 38 (10) https://doi.org/10.1029/2011GL047168.

Bernard, B., Samaniego, P., Mastin, L., Hernandez, S., Pino, G., Kibler, J., Encalada, M., Hidalgo, S., Vizuete, N., 2022. Forecasting and communicating the dispersion and fallout of ash during volcanic eruptions: lessons from the September 20, 2020 eruptive pulse at Sangay volcano, Ecuador. Front. Earth Sci. 10, 912835 https://doi.org/10.3389/feart.2022.912835.

Biass, S., Jenkins, S., Lallemant, D., Lim, T.N., Williams, G., Yun, S.-H., 2021. Remote sensing of volcanic impacts. In: Forecasting and Planning for Volcanic Hazards, Risks, and Disasters. Elsevier, pp. 473–491. https://doi.org/10.1016/B978-0-12-818082-2.00012-3.

Biggs, J., Pritchard, M.E., 2017. Global volcano monitoring: What does it mean when volcanoes deform? Elements 13 (1), 17–22. https://doi.org/10.2113/gselements.13.1.17.

Biggs, J., Wright, T., Lu, Z., Parsons, B., 2007. Multi-interferogram method for measuring interseismic deformation: Denali Fault, Alaska. Geophys. J. Int. 170 (3), 1165–1179. https://doi.org/10.1111/j.1365-246X.2007.03415.x.

Biggs, J., Mothes, P., Ruiz, M., Amelung, F., Dixon, T.H., Baker, S., Hong, S.-H., 2010. Stratovolcano growth by co-eruptive intrusion: The 2008 eruption of Tungurahua, Ecuador. Geophys. Res. Lett. 37, L21302. https://doi.org/10.1029/2010GL044942.

Biggs, J., Ebmeier, S., Aspinall, W.P., Lu, Z., Pritchard, M.E., Sparks, R.S.J., Mather, T.A., 2014. Global link between deformation and volcanic eruption quantified by satellite imagery. Nat. Commun. 5, 3471. https://doi.org/10.1038/ncomms4471.

Cassidy, M., Ebmeier, S.K., Helo, C., Watt, S.F.L., Caudron, C., Odell, A., Spaans, K., Kristianto, P., Triastuty, H., Gunawan, H., Castro, J.M., 2019. Explosive eruptions with little warning: experimental petrology and volcano monitoring observations from the 2014 eruption of Kelud, Indonesia. Geochem. Geophys. Geosyst. 20 (8), 4218–4247. https://doi.org/10.1029/2018GC008161.

Cayol, V., Cornet, F., 1997. 3D mixed boundary elements for elastostatic deformation field analysis. Int. J. Rock Mech. Min. Sci. 34 (2), 275–287. https://doi.org/10.1016/S0148-9062(96)00035-6.

Cayol, V., Cornet, F.H., 1998. Effects of topography on the interpretation of the deformation field of prominent volcanoes: application to Etna. Geophys. Res. Lett. 25 (11), 1979–1982. https://doi.org/10.1029/98GL51512.

Cayol, V., Dieterich, J.H., Okamura, A.T., Miklius, A., 2000. High magma storage rates before the 1983 eruption of Kilauea, Hawaii. Science 288 (5475), 2343–2346. https://doi.org/10.1126/science.288.5475.2343.

Cayol, V., Dabaghi, F., Fukushima, Y., Tridon, M., Smittarello, D., Bodart, O., Froger, J.-L., 2020a. DefVolc: Interface and web service for fast computation of volcano displacement. In: EGU General Assembly Conference Abstracts, EGU2020–22301. https://doi.org/10.5194/egusphere-egu2020-22301.

Cayol, V., Yo, F., Farshid, D., Olivier, B., Marine, T., Delphine, S., Dumont, Q., Froger, J.-L., Wauthier, C., Cattelain, C., Gouinaux, C., 2020b. DefVolc: tools for 3D inverse modelling of deformation data. https://doi.org/10.18145/defvolc.

Champenois, J., Pinel, V., Baize, S., Audin, L., Jomard, H., Hooper, A., Alvarado, A., Yepes, H., 2014. Large-scale inflation of Tungurahua volcano (Ecuador) revealed by Persistent Scatterers SAR interferometry. Geophys. Res. Lett. 41 (16), 5821–5828. https://doi.org/10.1002/2014GL060956.

Chaussard, E., Amelung, F., Aoki, Y., 2013. Characterization of open and closed volcanic systems in Indonesia and Mexico using InSAR time series. J. Geophys. Res. Solid Earth 118 (8), 3957–3969. https://doi.org/10.1002/jgrb.50288.

Chen, C., Zebker, H., 2002. Phase unwrapping for large SAR interferograms: statistical segmentation and generalized network models. IEEE Trans. Geosci. Remote Sens. 40 (8), 1709–1719. https://doi.org/10.1109/TGRS.2002.802453.

Coppola, D., Laiolo, M., Massimetti, F., Cigolini, C., 2019. Monitoring endogenous growth of open-vent volcanoes by balancing thermal and SO2 emissions data derived from space. Sci. Rep. 9 (1), 9394. https://doi.org/10.1038/s41598-019-45753-4.

Coppola, D., Valade, S., Masias, P., Laiolo, M., Massimetti, F., Campus, A., Aguilar, R., Anccasi, R., Apaza, F., Ccallata, B., Cigolini, C., Cruz, L.F., Finizola, A., Gonzales, K., Macedo, O., Miranda, R., Ortega, M., Paxi, R., Taipe, E., Valdivia, D., 2022. Shallow magma convection evidenced by excess degassing and thermal radiation during the dome-forming Sabancaya eruption (2012−2020). Bull. Volcanol. 84 (2), 16. https://doi.org/10.1007/s00445-022-01523-1.

Delgado, F., Pritchard, M.E., Basualto, D., Lazo, J., Córdova, L., Lara, L.E., 2016. Rapid reinflation following the 2011–2012 rhyodacite eruption at Cordón Caulle volcano (Southern Andes) imaged by InSAR: evidence for magma reservoir refill. Geophys. Res. Lett. 43 (18), 9552–9562. https://doi.org/10.1002/2016GL070066.

Di Traglia, F., De Luca, C., Manzo, M., Nolesini, T., Casagli, N., Lanari, R., Casu, F., 2021. Joint exploitation of space-borne and ground-based multitemporal InSAR measurements for volcano monitoring: the Stromboli volcano case study. Remote Sens. Environ. 260, 112441 https://doi.org/10.1016/j.rse.2021.112441.

Dogru, F., Albino, F., Biggs, J., 2023. Weather model based atmospheric corrections of Sentinel-1 InSAR deformation data at Turkish volcanoes. Geophys. J. Int. 234 (1), 280–296. https://doi.org/10.1093/gji/ggad070.

Doin, M.-P., Lodge, F., Guillaso, S., Jolivet, R., Lasserre, C., Ducret, G., Grandin, R., Pathier, E., Pinel, V., 2011. Presentation of the Small Baseline NSBAS Processing Chain on a Case Example: The Etna Deformation Monitoring from 2003 to 2010 Using Envisat Data.

Dualeh, E.W., Ebmeier, S., Wright, T.J., Albino, F., Naismith, A., Biggs, J., Ordoñez, P.A., Boogher, R.M., Roca, A., 2021. Analyzing explosive volcanic deposits from satellite-based radar backscatter, Volcán de Fuego, 2018. J. Geophys. Res. Solid Earth 126 (9). https://doi.org/10.1029/2021JB022250.

Dumont, Q., Sigmundsson, F., Parks, M.M., Drouin, V.J.P., Pedersen, G.B.M., Jónsdóttir, I., Hoskuldsson, A., Hooper, A., Spaans, K., Bagnardi, M., Gudmundsson, M.T., Barsotti, S., Jónsdóttir, K., Högnadóttir, T., Magnússon, E., Hjartardóttir, R., Dürig, T., Rossi, C., Oddsson, B., 2018. Integration of SAR data into monitoring of the 2014–2015 Holuhraun eruption, Iceland: Contribution of the Icelandic Volcanoes Supersite and the FutureVolc projects. Front. Earth Sci. 6, 231. https://doi.org/10.3389/feart.2018.00231.

Dumont, Q., Cayol, V., Froger, J.-L., 2024. Is stress modeling able to forecast intrusions and slip events at Piton de la Fournaise volcano? Earth Planet. Sci. Lett. 626, 118494 https://doi.org/10.1016/j.epsl.2023.118494.

Dzurisin, D., 2007. Analytical volcano deformation source models. In: Volcano Deformation. Springer, Berlin Heidelberg, pp. 279–304. https://doi.org/10.1007/978-3-540-49302-0_8.

Ebmeier, S., 2016. Application of independent component analysis to multitemporal InSAR data with volcanic case studies: ICA Analysis of InSAR Data. J. Geophys. Res. Solid Earth 121 (12), 8970–8986. https://doi.org/10.1002/2016JB013765.

Ebmeier, S., Biggs, J., Mather, T.A., Amelung, F., 2013a. Applicability of InSAR to tropical volcanoes: insights from Central America. In: Pyle, D.M., Mather, T.A., Biggs, J. (Eds.), Remote Sensing of Volcanoes and Volcanic Processes: Integrating Observation and Modelling, 380. Geological Society of London. https://doi.org/10.1144/SP380.2.

Ebmeier, S., Biggs, J., Mather, T.A., Amelung, F., 2013b. On the lack of InSAR observations of magmatic deformation at Central American volcanoes: InSAR measurements of the CAVA. J. Geophys. Res. Solid Earth 118 (5), 2571–2585. https://doi.org/10.1002/jgrb.50195.

Ebmeier, S., Biggs, J., Muller, C., Avard, G., 2014. Thin-skinned mass-wasting responsible for widespread deformation at Arenal volcano. Front. Earth Sci. 2 https://doi.org/10.3389/feart.2014.00035.

Ebmeier, S., Andrews, B.J., Araya, M.C., Arnold, D.W.D., Biggs, J., Cooper, C., Cottrell, E., Furtney, M., Hickey, J., Jay, J., Lloyd, R., Parker, A.L., Pritchard, M.E., Robertson, E., Venzke, E., Williamson, J.L., 2018. Synthesis of global satellite observations of magmatic and volcanic deformation: implications for volcano monitoring & the lateral extent of magmatic domains. J. Appl. Volcanol. 7 (1), 26. https://doi.org/10.1186/s13617-018-0071-3.

Eguez, A., Alvarado, A., Yepes, H., Machette, M., Costa, C., Dart, R., 2003. Database and Map of Quaternary Faults and Folds of Ecuador and its Offshore Regions. Open-File Report 03–289. U.S. Geological Survey.

ESA Team, 2015. Copernicus Open Access Hub.

Euillades, P.A., Euillades, L.D., Blanco, M.H., Velez, M.L., Grosse, P., Sosa, G.J., 2017. Co-eruptive subsidence and post-eruptive uplift associated with the 2011–2012 eruption

of Puyehue-Cordón Caulle, Chile, revealed by DInSAR. J. Volcanol. Geotherm. Res. 344, 257–269. https://doi.org/10.1016/j.jvolgeores.2017.06.023.
European Space Agency, 2021. Copernicus global digital elevation model. In: Distributed by OpenTopography. https://portal.opentopography.org/raster?opentopoID=OTSDEM.032021.4326.3.
Farr, T.G., Rosen, P.A., Caro, E., Crippen, R., Duren, R., Hensley, S., Kobrick, M., Paller, M., Rodriguez, E., Roth, L., Seal, D., Shaffer, S., Shimada, J., Umland, J., Werner, M., Oskin, M., Burbank, D., Alsdorf, D., 2007. The shuttle radar topography mission. Rev. Geophys. 45 (2), RG2004. https://doi.org/10.1029/2005RG000183.
Fialko, Y., Simons, M., Agnew, D., 2001. The complete (3-D) surface displacement field in the epicentral area of the 1999 M W 7.1 Hector Mine Earthquake, California, from space geodetic observations. Geophys. Res. Lett. 28 (16), 3063–3066. https://doi.org/10.1029/2001GL013174.
Francis, P., Oppenheimer, C., Stevenson, D., 1993. Endogenous growth of persistently active volcanoes. Nature 366 (6455), 554–557.
Fukushima, Y., 2005. Finding realistic dike models from interferometric synthetic aperture radar data: the February 2000 eruption at Piton de la Fournaise. J. Geophys. Res. 110 (B3), B03206. https://doi.org/10.1029/2004JB003268.
Fukushima, Y., Cayol, V., Durand, P., Massonnet, D., 2010. Evolution of magma conduits during the 1998–2000 eruptions of Piton de la Fournaise volcano, Réunion Island. J. Geophys. Res. Solid Earth 115 (B10), 2009JB007023. https://doi.org/10.1029/2009JB007023.
Gaddes, M.E., Hooper, A., Bagnardi, M., Inman, H., Albino, F., 2018. Blind signal separation methods for InSAR: the potential to automatically detect and monitor signals of volcanic deformation. J. Geophys. Res. Solid Earth 123 (11), 10226–10251. https://doi.org/10.1029/2018JB016210.
Gaddes, M.E., Hooper, A., Bagnardi, M., 2019. Using machine learning to automatically detect volcanic unrest in a time series of interferograms. J. Geophys. Res. Solid Earth 124 (11), 12304–12322. https://doi.org/10.1029/2019JB017519.
Galetto, F., 2023. Complex paths of magma propagation at Fernandina (Galápagos): The coexistence of circumferential and radial dike intrusion during the January 2020 eruption. Bull. Volcanol. 85 (12), 71. https://doi.org/10.1007/s00445-023-01688-3.
Gallant, E., Deng, F., Connor, C., Dixon, T., Xie, S., Saballos, J., Gutiérrez, C., Myhre, D., Connor, L., Zayac, J., LaFemina, P., Charbonnier, S., Richardson, J., Malservisi, R., Thompson, G., 2020. Deep and rapid thermomechanical erosion by a small-volume lava flow. Earth Planet. Sci. Lett. 537, 116163 https://doi.org/10.1016/j.epsl.2020.116163.
Garcia, M.O., 2015. How and why Hawaiian volcanism has become pivotal to our understanding of volcanoes from their source to the surface. In: Carey, R., Cayol, V., Poland, M., Weis, D. (Eds.), Geophysical Monograph Series. Wiley, pp. 1–18. https://doi.org/10.1002/9781118872079.ch1.
Hall, M., 1977. El volcanismo en el Ecuador. IPGH, Sección Nacional del Ecuador.
Hall, M., Samaniego, P., Le Pennec, J., Johnson, J., 2008. Ecuadorian Andes volcanism: a review of Late Pliocene to present activity. J. Volcanol. Geotherm. Res. 176 (1), 1–6. https://doi.org/10.1016/j.jvolgeores.2008.06.012.
Hamling, I.J., Hreinsdóttir, S., Bannister, S., Palmer, N., 2016. Off-axis magmatism along a subaerial back-arc rift: observations from the Taupo Volcanic Zone, New Zealand. Sci. Adv. 2 (6), e1600288 https://doi.org/10.1126/sciadv.1600288.
Hamlyn, J., Wright, T., Walters, R., Pagli, C., Sansosti, E., Casu, F., Pepe, S., Edmonds, M., McCormick Kilbride, B., Keir, D., Neuberg, J., Oppenheimer, C., 2018. What causes subsidence following the 2011 eruption at Nabro (Eritrea)? Progr. Earth Planet. Sci. 5 (1), 31. https://doi.org/10.1186/s40645-018-0186-5.
Hanssen, R.F., van Leijen, F.J., van Zwieten, G.J., Delft, T., Bremmer, C., Dortland, S., Kleuskens, M., 2008. Product Validation: Validation in the Amsterdam and Alkmaar Area, p. 85.
Harris, A.J., Flynn, L.P., Rothery, D.A., Oppenheimer, C., Sherman, S.B., 1999. Mass flux measurements at active lava lakes: implications for magma recycling. J. Geophys. Res. Solid Earth 104 (B4), 7117–7136. https://doi.org/10.1029/1999JB900018.
Hautmann, S., Sacks, I.S., Linde, A.T., Roberts, M.J., 2017. Magma buoyancy and volatile ascent driving autocyclic eruptivity at Hekla Volcano (Iceland): Autocyclic eruptivity at Hekla Volcano. Geochem. Geophys. Geosyst. 18 (9), 3517–3529. https://doi.org/10.1002/2017GC007061.
Herrería, F., 2020. Trabajo de titulación previo a la obtención del título de Ingeniera Geóloga (Enginering thesis). Escuela Politécnica Nacional. https://bibdigital.epn.edu.ec/handle/15000/21880.
Hickey, J., Lloyd, R., Biggs, J., Arnold, D., Mothes, P., Muller, C., 2020. Rapid localized flank inflation and implications for potential slope instability at Tungurahua volcano, Ecuador. Earth Planet. Sci. Lett. 534, 116104 https://doi.org/10.1016/j.epsl.2020.116104.
Hidalgo, S., Battaglia, J., Arellano, S., Steele, A., Bernard, B., Bourquin, J., Galle, B., Arrais, S., Vásconez, F., 2015. SO2 degassing at Tungurahua volcano (Ecuador) between 2007 and 2013: transition from continuous to episodic activity. J. Volcanol. Geotherm. Res. 298, 1–14. https://doi.org/10.1016/j.jvolgeores.2015.03.022.
Hidalgo, S., Vásconez, F.J., Battaglia, J., Bernard, B., Espín, P., Valade, S., Naranjo, M.-F., Campion, R., Salgado, J., Córdova, M., Almeida, M., Hernández, S., Pino, G., Gaunt, E., Bell, A., Mothes, P., Ruiz, M., 2022. Sangay volcano (Ecuador): the opening of two new vents, a drumbeat seismic sequence and a new lava flow in late 2021. Volcanica 5 (2), 295–311. https://doi.org/10.30909/vol.05.02.295311.
Hidalgo, S., Bernard, B., Mothes, P., Ramos, C., Aguilar, J., Andrade, D., Samaniego, P., Yepes, H., Hall, M., Alvarado, A., Segovia, M., Ruiz, M., Ramón, P., Vaca, M., 2024. Hazard Assessment and Monitoring of Ecuadorian volcanoes: Challenges and Progress During Four Decades since IG-EPN Foundation.
Himematsu, Y., Ozawa, T., Aoki, Y., 2020. Coeruptive and posteruptive crustal deformation associated with the 2018 Kusatsu-Shirane phreatic eruption based on PALSAR-2 time series analysis. Earth Planets Space 72 (1), 116. https://doi.org/10.1186/s40623-020-01247-6.
Hooper, A., 2009. A Statistical-cost Approach to Unwrapping the Phase of InSAR Time Series.
Hooper, A., Bekaert, D., Spaans, K., Arıkan, M., 2012. Recent advances in SAR interferometry time series analysis for measuring crustal deformation. Tectonophysics 514–517, 1–13. https://doi.org/10.1016/j.tecto.2011.10.013.
Hyvärinen, A., Karhunen, J., Oja, E., 2004. Independent Component Analysis. John Wiley & Sons, New York.
IGEPN. (2022). Informe Volcánico Especial – Sangay – N° 2022–001. Technical Report. Retrieved from https://www.igepn.edu.ec/servicios/noticias/1928-informe-volcanico-especial-sangay-n-2022-001.
IG-EPN, 2021. Informe Especial del Volcán Sangay - 2020 - N ° 5. Technical Report. Retrieved from. https://informes.igepn.edu.ec/igepn-registro-web/pages/public/InformeGenerado.jsf?directorio=25446.
Jung, J., Kim, D.-J., Lavalle, M., Yun, S.-H., 2016. Coherent change detection using InSAR temporal decorrelation model: a case study for volcanic ash detection. IEEE Trans. Geosci. Remote Sens. 54 (10), 5765–5775. https://doi.org/10.1109/TGRS.2016.2572166.
Kilbride, B.M., Edmonds, M., Biggs, J., 2016. Observing eruptions of gas-rich compressible magmas from space. Nat. Commun. 7 (1), 13744. https://doi.org/10.1038/ncomms13744.
Lazecky, M., Spaans, K., González, P.J., Maghsoudi, Y., Morishita, Y., Albino, F., Elliott, J., Greenall, N., Hatton, E., Hooper, A., Juncu, D., McDougall, A., Walters, R. J., Watson, C.S., Weiss, J.R., Wright, T.J., 2020. LiCSAR: An automatic InSAR tool for measuring and monitoring tectonic and volcanic activity. Remote Sens. 12 (15), 2430. https://doi.org/10.3390/rs12152430.
Lin, Y.-N.N., Kositsky, A.P., Avouac, J.-P., 2010. PCAIM joint inversion of InSAR and ground-based geodetic time series: Application to monitoring magmatic inflation beneath the Long Valley Caldera. Geophys. Res. Lett. 37 (23) https://doi.org/10.1029/2010GL045769.
Locke, C.A., Rymer, H., Cassidy, J., 2003. Magma transfer processes at persistently active volcanoes: Insights from gravity observations. J. Volcanol. Geotherm. Res. 127 (1–2), 73–86. https://doi.org/10.1016/S0377-0273(03)00179-3.
Maghsoudi, Y., Lazecky, M., Ansari, H., Hooper, A.J., Wright, T.J., 2021. Investigation of the phase bias in the short term interferograms. In: 2021 IEEE International Geoscience and Remote Sensing Symposium (IGARSS). IEEE, pp. 3380–3383. https://doi.org/10.1109/IGARSS47720.2021.9553631.
Malinverni, E.S., Sandwell, D.T., Tassetti, A.N., Cappelletti, L., 2014. InSAR decorrelation to assess and prevent volcanic risk. Europ. J. Remote Sens. 47 (1), 537–556. https://doi.org/10.5721/EuJRS20144730.
Mania, R., Walter, T.R., Belousova, M., Belousov, A., Senyukov, S.L., 2019. Deformations and morphology changes associated with the 2016–2017 eruption sequence at Bezymianny Volcano, Kamchatka. Remote Sens. 11 (11), 1278. https://doi.org/10.3390/rs11111278.
Maubant, L., Pathier, E., Daout, S., Radiguet, M., Doin, M., Kazachkina, E., Kostoglodov, V., Cotte, N., Walpersdorf, A., 2020. Independent component analysis and parametric approach for source separation in InSAR time series at regional scale: application to the 2017–2018 slow slip event in Guerrero (Mexico). J. Geophys. Res. Solid Earth 125 (3).
Monzier, M., Robin, C., Samaniego, P., Hall, M.L., Cotten, J., Mothes, P., Arnaud, N., 1999. Sangay volcano, Ecuador: structural development, present activity and petrology. Journal of Volcanology and Geothermal Research 90 (1–2), 49–79. https://doi.org/10.1016/S0377-0273(99)00021-9.
Morales, R., Amelung, F., Mothes, P., 2016. Volcano deformation survey over the Northern and Central Andes with ALOS InSAR time series. Geochem. Geophys. Geosyst. 17, 2869–2883. https://doi.org/10.1002/2016GC006393.
Morales, R., Amelung, F., Mothes, P., Hong, S.-H., Nocquet, J.-M., Jarrin, P., 2017. Ground deformation before the 2015 eruptions of Cotopaxi volcano detected by InSAR. Geophys. Res. Lett. 44, 6607–6615. https://doi.org/10.1002/2017GL073720.
Morgado, E., Morgan, D.J., Castruccio, A., et al., 2019. Old magma and a new, intrusive trigger: using diffusion chronometry to understand the rapid-onset Calbuco eruption, April 2015 (Southern Chile). Contrib Mineral Petrol 174, 61. https://doi.org/10.1007/s00410-019-1596-0.
Morishita, Y., 2021. Nationwide urban ground deformation monitoring in Japan using Sentinel-1 LiCSAR products and LiCSBAS. Prog Earth Planet Sci 8, 6. https://doi.org/10.1186/s40645-020-00402-7.
Morishita, Y., Lazecky, M., Wright, T.J., Weiss, J.R., Elliott, J.R., Hooper, A., 2020. LiCSBAS: An Open-Source InSAR Time Series Analysis Package Integrated with the LiCSAR Automated Sentinel-1 InSAR Processor. Remote Sensing 12 (3), 424. https://doi.org/10.3390/rs12030424.
Motagh, M., Shamshiri, R., Haghshenas Haghighi, M., Wetzel, H.-U., Akbari, B., Nahavandchi, H., Roessner, S., Arabi, S., 2017. Quantifying groundwater exploitation induced subsidence in the Rafsanjan plain, southeastern Iran, using InSAR time-series and in situ measurements. Eng. Geol. 218, 134–151. https://doi.org/10.1016/j.enggeo.2017.01.011.
Mothes, P.A., Yepes, H.A., Hall, M.L., Ramón, P.A., Steele, A.L., Ruiz, M.C., 2015. The scientific–community interface over the fifteen-year eruptive episode of Tungurahua Volcano, Ecuador. J. Appl. Volcanol. 4 (1), 9. https://doi.org/10.1186/s13617-015-0025-y.
Muller, C., Biggs, J., Ebmeier, S.K., Mothes, P., Palacios, P.B., Jarrín, P., Edmonds, M., Ruiz, M., 2018. Temporal evolution of the magmatic system at Tungurahua Volcano, Ecuador, detected by geodetic observations. J. Volcanol. Geotherm. Res. 368, 63–72. https://doi.org/10.1016/j.jvolgeores.2018.11.004.
Ofeigsson, B.G., Hooper, A., Sigmundsson, F., Sturkell, E., Grapenthin, R., 2011. Deep magma storage at Hekla volcano, Iceland, revealed by InSAR time series analysis. J. Geophys. Res. 116 (B5), B05401. https://doi.org/10.1029/2010JB007576.

Ordóñez, J., Vallejo, S., Bustillos, J., Hall, M., Andrade, D., Hidalgo, S., Samaniego, P., 2013. Volcán Sangay, peligros potenciales. [Report].
Parks, M., Biggs, J., Mather, T., Pyle, D., Amelung, F., Monsalve, M., Medina, L.N., 2011. Co-eruptive subsidence at Galeras identified during an InSAR survey of Colombian volcanoes (2006–2009). J. Volcanol. Geotherm. Res. 202 (3–4), 228–240. https://doi.org/10.1016/j.jvolgeores.2011.02.007.
Pinel, V., Hooper, A., De la Cruz-Reyna, S., Reyes-Davila, G., Doin, M., Bascou, P., 2011. The challenging retrieval of the displacement field from InSAR data for andesitic stratovolcanoes: case study of Popocatepetl and Colima Volcano, Mexico. J. Volcanol. Geotherm. Res. 200 (1–2), 49–61. https://doi.org/10.1016/j.jvolgeores.2010.12.002.
Pinel, V., Poland, M., Hooper, A., 2014. Volcanology: lessons learned from synthetic aperture radar imagery. J. Volcanol. Geotherm. Res. 289, 81–113. https://doi.org/10.1016/j.jvolgeores.2014.10.010.
Pinel, V., Albino, F., Bato, G., Lundgren, P., 2022. Volcanology: The crucial contribution of surface displacement measurements from space for understanding and monitoring volcanoes. In: Volcanology: A Comprehensive Approach. John Wiley & Sons, pp. 247–281. https://doi.org/10.1002/9781119986843.ch8.
Planet Team, 2017. Planet application program interface. In: Space for Life on Earth. Retrieved from. https://www.planet.com/.
Pollard, D.D., Delaney, P.T., Duffield, W.A., Endo, E.T., Okamura, A.T., 1983. Surface deformation in volcanic rift zones. In: Morgan, P., Baker, B. (Eds.), Processes of Continental Rifting, 19. Elsevier, pp. 541–584. https://doi.org/10.1016/B978-0-444-42198-2.50036-5.
Pritchard, M.E., Biggs, J., Wauthier, C., Sansosti, E., Arnold, D.W.D., Delgado, F., Ebmeier, S.K., Henderson, S.T., Stephens, K., Cooper, C., Wnuk, K., Amelung, F., Aguilar, V., Mothes, P., Macedo, O., Lara, L.E., Poland, M.P., Zoffoli, S., 2018. Towards coordinated regional multisatellite InSAR volcano observations: results from the Latin America pilot project. J. Appl. Volcanol. 7 (1), 5. https://doi.org/10.1186/s13617-018-0074-0.
Purcell, V., Reddin, E., Ebmeier, S., González, P.J., Watson, A., Morishita, Y., Elliott, J., 2022. Nearly three centuries of lava flow subsidence at Timanfaya, Lanzarote. Geochem. Geophys. Geosyst. 23 (10) https://doi.org/10.1029/2022GC010576.
Reath, K., Pritchard, M., Poland, M., Delgado, F., Carn, S., Coppola, D., Andrews, B., Ebmeier, S.K., Rumpf, E., Henderson, S., Baker, S., Lundgren, P., Wright, R., Biggs, J., Lopez, T., Wauthier, C., Moruzzi, S., Alcott, A., Wessels, R., Griswold, J., Ogburn, S., Loughlin, S., Meyer, F., Vaughan, G., Bagnardi, M., 2019. Thermal, deformation, and degassing remote sensing time series (CE 2000–2017) at the most active volcanoes in Latin America: implications for volcanic systems. J. Geophys. Res. Solid Earth 124 (1), 195–218. https://doi.org/10.1029/2018JB016199.
Reath, K., Pritchard, M., Biggs, J., Andrews, B., Ebmeier, S.K., Bagnardi, M., Girona, T., Lundgren, P., Lopez, T., Poland, M., 2020. Using conceptual models to relate multiparameter satellite data to subsurface volcanic processes in Latin America. Geochem. Geophys. Geosyst. 21 (1), e2019GC008494 https://doi.org/10.1029/2019GC008494.
Reddin, E., Ebmeier, S.K., Rivalta, E., et al., 2023. Magmatic connectivity among six Galapagos volcanoes revealed by satellite geodesy. Nat. Commun. 14, 6614. https://doi.org/10.1038/s41467-023-42157-x.
Remy, D., Chen, Y., Froger, J.L., Bonvalot, S., Cordoba, L., Fustos, J., 2015. Revised interpretation of recent InSAR signals observed at Llaima volcano (Chile). Geophys. Res. Lett. 42 (10), 3870–3879. https://doi.org/10.1002/2015GL063872.
Reverso, T., Vandemeulebrouck, J., Jouanne, F., Pinel, V., Villemin, T., Sturkell, E., Bascou, P., 2014. A two-magma chamber model as a source of deformation at Grímsvötn Volcano, Iceland. J. Geophys. Res. Solid Earth 119 (6), 4666–4683. https://doi.org/10.1002/2013JB010569.
Rivalta, E., Segall, P., 2008. Magma compressibility and the missing source for some dike intrusions. Geophys. Res. Lett. 35 (4), L04306. https://doi.org/10.1029/2007GL032521.
Salzer, J.T., Nikkhoo, M., Walter, T.R., Sudhaus, H., Reyes-Dávila, G., Bretón, M., Arámbula, R., 2014. Satellite radar data reveal short-term pre-explosive displacements and a complex conduit system at Volcán de Colima, Mexico. Front. Earth Sci. 2 https://doi.org/10.3389/feart.2014.00012.
Sandwell, D., Myer, D., Shimada, M., Brooks, B., Foster, J., 2007. Vector deformation maps of the Father's Day intrusion at Kilauea: Constraints on magma injection. In: AGU Fall Meeting Abstracts, 2007. V53A–1136.
Schaefer, L.N., Di Traglia, F., Chaussard, E., Lu, Z., Nolesini, T., Casagli, N., 2019. Monitoring volcano slope instability with Synthetic Aperture Radar: a review and new data from Pacaya (Guatemala) and Stromboli (Italy) volcanoes. Earth Sci. Rev. 192, 236–257. https://doi.org/10.1016/j.earscirev.2019.03.009.
Scheiber, R., Moreira, A., 2000. Coregistration of interferometric SAR images using spectral diversity. IEEE Trans. Geosci. Remote Sens. 38 (5), 2179–2191. https://doi.org/10.1109/36.868876.
Shreve, T., Grandin, R., Boichu, M., 2022. Reservoir depressurization driven by passive gas emissions at Ambrym volcano. Earth Planet. Sci. Lett. 584, 117512 https://doi.org/10.1016/j.epsl.2022.117512.
Sigmundsson, F., Einarsson, P., Bilham, R., 1992. Magma chamber deflation recorded by the global positioning system: the Hekla 1991 Eruption. Geophys. Res. Lett. 19 (14), 1483–1486. https://doi.org/10.1029/92GL01636.
Sigmundsson, F., Hreinsdóttir, S., Hooper, A., Árnadóttir, T., Pedersen, R., Roberts, M.J., Óskarsson, N., Auriac, A., Decriem, J., Einarsson, P., Geirsson, H., Hensch, M., Ófeigsson, B.G., Sturkell, E., Sveinbjörnsson, H., Feigl, K.L., 2010. Intrusion triggering of the 2010 Eyjafjallajökull explosive eruption. Nature 468 (7322), 426–430. https://doi.org/10.1038/nature09558.
Simons, M., Rosen, P., 2015. Interferometric synthetic Aperture Radar Geodesy. In: Treatise on Geophysics. Elsevier, pp. 339–385. https://doi.org/10.1016/B978-0-444-53802-4.00061-0.
Spaans, K., Hooper, A., 2016. InSAR processing for volcano monitoring and other near-real time applications: InSAR processing for volcano monitoring. J. Geophys. Res. Solid Earth 121 (4), 2947–2960. https://doi.org/10.1002/2015JB012752.
Sparks, R.S.J., 2003. Forecasting volcanic eruptions. Earth Planet. Sci. Lett. 210 (1–2), 1–15. https://doi.org/10.1016/S0012-821X(03)00124-9.
Sparks, R.S.J., Cashman, K.V., 2017. Dynamic magma systems: implications for forecasting volcanic activity. Elements 13 (1), 35–40. https://doi.org/10.2113/gselements.13.1.35.
Stephens, K., Ebmeier, S., Young, N., Biggs, J., 2017. Transient deformation associated with explosive eruption measured at Masaya volcano (Nicaragua) using Interferometric Synthetic Aperture Radar. J. Volcanol. Geotherm. Res. 344, 212–223. https://doi.org/10.1016/j.jvolgeores.2017.05.014.
Tilling, R.I., Dvorak, J.J., 1993. Anatomy of a basaltic volcano. Nature 363 (6425), 125–133.
Valverde, V., 2014. Los depósitos de avalancha de escombros provenientes del volcán Sangay: Caracterización petrográfica - geoquímica. PhD thesis. Escuela Politécnica Nacional. Retrieved from. https://bibdigital.epn.edu.ec/handle/15000/8950.
Valverde, V., Mothes, P.A., Beate, B., Bernard, J., 2021. Enormous and far-reaching debris avalanche deposits from Sangay volcano (Ecuador): Multidisciplinary study and modeling the 30 ka sector collapse. J. Volcanol. Geotherm. Res. 411, 107–172. https://doi.org/10.1016/j.jvolgeores.2021.107172.
Vásconez, F.J., Hidalgo, S., Battaglia, J., Hernandez, S., Bernard, B., Coppola, D., Valade, S., Ramón, P., Arellano, S., Liorzou, C., Almeida, M., Ortíz, M., Córdoba, J., Vásconez Müller, A., 2022. Linking ground-based data and satellite monitoring to understand the last two decades of eruptive activity at Sangay volcano, Ecuador. Bull. Volcanol. 84 (5), 49. https://doi.org/10.1007/s00445-022-01560-w.
Volcanes del Ecuador, 2020. Historia de la quebrada suroriental del volcán Sangay. Retrieved from. http://ceniza-ecuador.over-blog.com/2020/10/a71-historia-de-la-quebrada-suroriental-del-volcan-sangay.html.
Watson, A.R., Elliott, J.R., Walters, R.J., 2022. Interseismic strain accumulation across the Main Recent Fault, SW Iran, from Sentinel-1 InSAR observations. J. Geophys. Res. Solid Earth 127 (2). https://doi.org/10.1029/2021JB022674.
Wauthier, C., Cayol, V., Kervyn, F., d'Oreye, N., 2012. Magma sources involved in the 2002 Nyiragongo eruption, as inferred from an InSAR analysis. J. Geophys. Res. Solid Earth 117 (B5). https://doi.org/10.1029/2011JB008257, 2011JB008257.
Wegmüller, U., Werner, C., Strozzi, T., Wiesmann, A., Frey, O., Santoro, M., 2016. Sentinel-1 support in the GAMMA software. Procedia Comp. Sci. 100, 1305–1312. https://doi.org/10.1016/j.procs.2016.09.246.
Werner, C., Wegmüller, U., Strozzi, T., Wiesmann, A., 2000. GAMMA SAR and Interferometric Processing Software.
Westerhoff, R., Steyn-Ross, M., 2020. Explanation of InSAR phase disturbances by seasonal characteristics of soil and vegetation. Remote Sens. 12 (18), 3029. https://doi.org/10.3390/rs12183029.
Wittmann, W., Sigmundsson, F., Dumont, S., Lavallée, Y., 2017. Postemplacement cooling and contraction of lava flows: InSAR observations and a thermal model for lava fields at Hekla volcano, Iceland. J. Geophys. Res. Solid Earth 122 (2), 946–965. https://doi.org/10.1002/2016JB013444.
Wright, T., Parsons, B.E., Lu, Z., 2004. Toward mapping surface deformation in three dimensions using InSAR. Geophys. Res. Lett. https://doi.org/10.1029/2003GL018827.
Wright, T., Sigmundsson, F., Pagli, C., Belachew, M., Hamling, I.J., Brandsdóttir, B., Keir, D., Pedersen, R., Ayele, A., Ebinger, C., Einarsson, P., Lewi, E., Calais, E., 2012. Geophysical constraints on the dynamics of spreading centres from rifting episodes on land. Nat. Geosci. 5 (4), 242–250. https://doi.org/10.1038/ngeo1428.
Xu, W., Rivalta, E., Li, X., 2017. Magmatic architecture within a rift segment: articulate axial magma storage at Erta Ale volcano, Ethiopia. Earth Planet. Sci. Lett. 476, 79–86. https://doi.org/10.1016/j.epsl.2017.07.051.
Yip, S.T.H., Biggs, J., Albino, F., 2019. Reevaluating volcanic deformation using atmospheric corrections: Implications for the magmatic system of Agung Volcano, Indonesia. Geophys. Res. Lett. 46 (23), 13704–13711. https://doi.org/10.1029/2019GL085233.
Yip, S.T.H., Biggs, J., Edmonds, M., Liggins, P., Shorttle, O., 2022. Contrasting volcanic deformation in arc and ocean island settings due to exsolution of magmatic water. Geochem. Geophys. Geosyst. 23 (7) https://doi.org/10.1029/2022GC010387.
Yu, C., Li, Z., Penna, N.T., Crippa, P., 2018. Generic atmospheric correction model for interferometric synthetic aperture radar observations. J. Geophys. Res. Solid Earth 123 (10), 9202–9222. https://doi.org/10.1029/2017JB015305.